DLR-IB-AT-KP-2021-38

Large Eddy Simulation of a Generic Impinging Jet Configuration

Patrick Hermsmeyer

Deutsches Zentrum
DLR für Luft- und Raumfahrt

Abstract

The aim of this work is to generate comprehensive numerical data for multiple impinging jets in cross-flow. Therefore, several Reynolds-averaged Navier-Stokes (RANS) simulations and large eddy simulations (LES) are carried out for an in-row arrangement of nine impinging jets with a jet Reynolds number of ≈10,000. This data should contribute to a better understanding of the heat transport processes being involved. The RANS and LES studies are conducted using the computational fluid dynamics (CFD) solver TRACE (Turbomachinery Research Aerodynamic Computational Environment), which is being developed by the German Aerospace Center (DLR).

In the RANS study, grid convergence is verified using the grid convergence index (GCI) method [7]. A sensitivity study indicates that changes in the heat flux have only a minor influence on the overall heat transfer characteristics. However, the effects of changes in mass flow are significant.

For the LES, sufficient grid resolution is verified by comparing the filter length scales to the Kolmogorov scales. In terms of statistical convergence, the velocity and turbulent kinetic energy show large sampling errors caused by the limited number of through flows.

Concerning global heat transfer, the RANS simulations and LES show only small deviations in Nusselt number well matching with empirical correlations reported in the literature. However, the predicted local Nusselt numbers and velocity fields significantly deviate between RANS simulations and LES.

In future studies at DLR, the obtained numerical data will be used for the validation of current numerical design methods and turbulence models for impingement cooling.

Contents

List of Figures

List of Tables

List of Symbols

Latin Symbols

Symbol	Description	Unit
a	Model constant	-
a	Speed of sound	m s^{-1}
b	Body force	N
c_p	Specific heat capacity at constant pressure	J kg^{-1} K^{-1}
c_v	Specific heat capacity at constant volume	J kg^{-1} K^{-1}
C	Model constant	
CFL	Courant-Friedrichs-Lewy number	-
CI	Confidence interval	
d	Sample index	-
$d*$	Sample index at end of initial transient	-
D	Nozzle diameter	m
D_ω	Cross-diffusion term	kg m^{-3} s^{-2}
e	Estimated error	
e	Specific internal energy	J kg^{-1}
E	Energy	J
f	Frequency	s^{-1}
f_{cut}	Cut-off frequency	s^{-1}
f_β	Model coefficient	-
F	Blending function	-
$\tilde{\hat{g}}_{ij}$	Gradient velocity tensor	s^{-1}
G	Filter function	-
GCI	Grid convergence index	-
h	Representative cell size	m

h	Specific enthalpy	J kg^{-1}
H	Nozzle height	m
k	Specific turbulent kinetic energy	J kg^{-1}
k	Wave number	1 m^{-1}
l	Length	m
$\dot{m}$	Mass flow	kg/s
Ma	Mach number	-
Ma_T	Turbulent Mach number	-
Ma_{T0}	Model constant	-
$n_{equations}$	Number of equations	-
N	Total number of cells	-
N	Total number of samples	-
N_d	Minimal number of samples between two independent observations	-
Nu	Nusselt number	-
p	Apparent order	-
p	Pressure	Pa
Pr	Prandtl number	-
PSD	Power Spectral Density	m^2/s
q	Specific heat flux	W m^{-2}
r	Grid refinement factor	-
R	Gas constant	J kg^{-1} K^{-1}
R	Model constant	-
R	Residual vector	
Re	Reynolds number	-
Re_T	Turbulent Reynolds number	-
s	Spacing (or pitch)	m
S	Rate of strain	s^{-1}
S	Source term	
S_{ij}^d	Operator introduced for WALE model	s^{-2}
t	Time	s
t'	Time	s
T	Temperature	K
u, v, w	Velocities in Cartesian coordinate system	m s^{-1}

$\|u\|$	Velocity magnitude	m s^{-1}
u_τ	Shear velocity	m s^{-1}
V	Cell volume	m^3
W	Channel width	m
x, y, z	Cartesian coordinate	m
y^+	Non-dimensional distance wall coordinate	-
Y	Dissipation term	

Greek Symbols

Symbol	Description	Unit
α	Model constant	-
α	Heat transfer coefficient	W m^{-2} K^{-1}
α_i	Subgrid terms of the energy equation	kg m^{-1} s^{-3}
β	Model constant	-
δ_{ij}	Kronecker delta	-
Δ_{cut}	Spatial cut-off scale	m
Δx, Δy, Δz	Cell dimensions	m
$\Delta\tau$	Pseudo time step	s
ε	Dissipation rate	m^2 s^{-3}
ζ	Model constant	-
κ	Heat capacity ratio	-
λ	Thermal conductivity	W m^{-1} K^{-1}
μ	Dynamic viscosity	Pa s
μ_T	Dynamic eddy viscosity	Pa s
ν	Kinematic viscosity	m^2 s^{-1}
ν_{sgs}	Kinematic subgrid viscosity	m^2 s^{-1}
ν_T	Kinematic eddy viscosity	m^2 s^{-1}
ξ	Coordinate	m
ρ	Density	kg m^{-3}
σ	Model constant	-
χ_ω	Model coefficient	-
τ	Stress	Pa

τ_{ij}^{F}	Favre-averaged specific Reynolds stress tensor	$\mathrm{m}^2\ \mathrm{s}^{-2}$
τ_{ij}^{T}	Turbulent stress tensor	$\mathrm{m}^2\ \mathrm{s}^{-2}$
ϕ	General flow variable	
ω	Specific dissipation rate	s^{-1}

Subscripts and Superscripts

Symbol	Description
$\square_{a}$	Approximated
$\square_{abs}$	Absolute value
$\square_{c}$	Characteristic dimension
$\square_{d}$	Variable relating to sample index
$\square^{d}$	Deviatoric part
$\square_{ext}$	Extrapolated variable
$\square_{hp}$	Variable relating to heating plate
$\square_{inlet}$	Variable relating to inlet
$\square_{mean}$	Mean value
$\square_{nozzle}$	Variable relating to nozzle
$\square_{nozzle7}$	Flow variable averaged within nozzle 7
$\square_{N}$	Variable relating to total number of samples
$\square_{target}$	Target value
$\square_{wall}$	Variable relating to wall
$\square_{\eta}$	Kolmogorov scale
$\square_{0}$	Initial value
$\square_{0}$	Reference value

Diacritics

Symbol	Description
$\tilde{\square}$	Favre-averaged component
$\tilde{\hat{\square}}$	Favre-filtered component
$\hat{\square}$	Filtered component

$\square''$	Fluctuating component based on Favre-averaging
$\square'$	Fluctuating component based on Reynolds-averaging
$\breve{\square}$	Function of filtered variable
$\bar{\square}$	Mean value
$\square''''$	Non-resolved component based on Favre-filtering
$\square'''$	Non-resolved component based on filtering
$\bar{\square}$	Reynolds-averaged component

Abbreviations

Abbreviation	Description
CFD	Computational Fluid Dynamics
DLR	German Aerospace Center
DNS	Direct Numerical Simulation
GCI	Grid Convergence Index
LES	Large Eddy Simulation
MUSCL	Monotonic Upstream-centered Scheme for Conservation Laws
PSD	Power Spectral Density
RANS	Reynolds-Averaged Navier-Stokes
SST	Shear Stress Transport
TRACE	Turbomachinery Research Aerodynamic Computational Environment
WALE	Wall-Adapting Local Eddy-viscosity

1 Introduction

The main application fields for gas turbines are the aviation and power generation industries. One of the primary goals of gas turbine development is to increase their efficiency, which mainly depends on the turbine inlet temperature and compressor pressure ratio.[35] In order to achieve high efficiency, the turbine inlet temperature is increased above the permissible metal temperature of the turbine blades and vanes. Consequently, they have to be cooled using various external and internal cooling mechanisms (see Figure 1.1).[24]

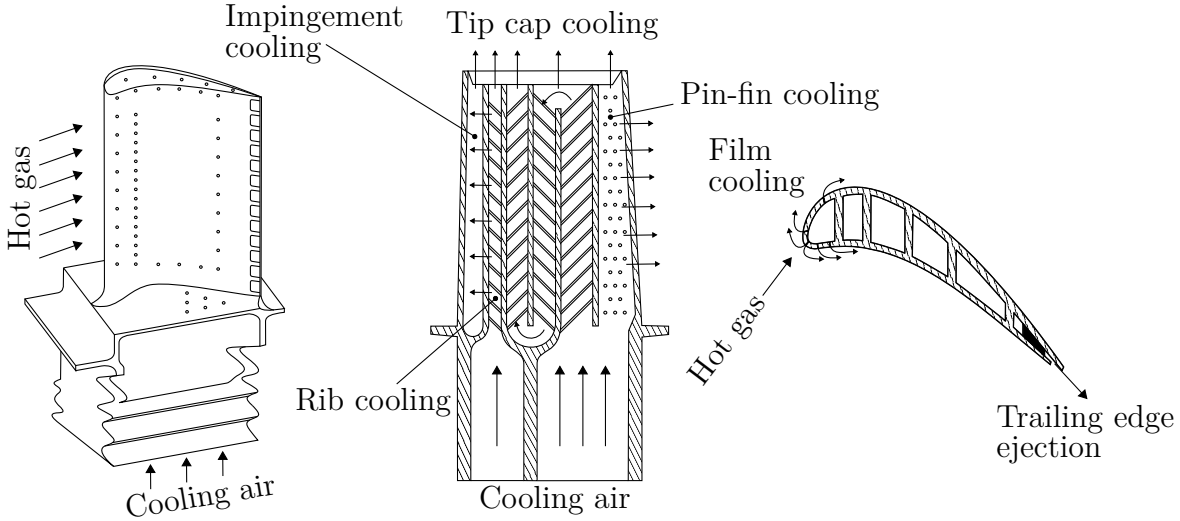

Figure 1.1: Three-dimensional and cross-sectional view of a turbine blade that is equipped with different cooling mechanisms

Film cooling is an external cooling mechanism, where a thin layer of cooling air insulates the turbine blade from the hot combustion gas stream. Of all cooling mechanisms, this is the most efficient one. However, it is typically combined with internal cooling mechanisms, such as *convection cooling* or *impingement cooling*. Convection cooling implies that the coolant passes over the inner surface of the blade, which is equipped with ribs or pin-fins. The principle of impingement cooling is that the coolant is ejected of small holes from an insert inside the blade and then impacts its outer wall.[29] At a given maximum flow velocity, this mechanism can be up to three times more efficient compared to conventional

convection cooling [44].

The numerical methods used to predict the heat transport processes involved in impingement cooling, e.g., RANS simulations, are still relatively inaccurate, which leads to conservative design processes. As a consequence, unnecessarily high amounts of cooling air are taken from the compressor, resulting in undesired efficiency losses for the gas turbine. Therefore, it is important to gain a better understanding of the local heat transport characteristics of impingement cooling and the inaccuracies of current design methods.

Numerous experimental and numerical studies on different impinging jet configurations are described in the literature. Dewan et al. [9] provide a comprehensive review of several investigations on single impinging jets, which were carried out using direct numerical simulation (DNS) and large eddy simulation (LES). The reviews by Zuckerman and Lior [44] as well as Weigand and Spring [40] contain various empirical correlations for the heat transfer characteristics of single and multiple impinging jets. Brakmann [6] investigated two in-row arrangements of multiple impinging jets experimentally as well as numerically using Reynolds-averaged Navier-Stokes (RANS) simulations.

The aim of this work is to provide comprehensive numerical data on a multiple impinging jet configuration. This data should contribute to a better understanding of the heat transport processes, but also serve the validation and improvement of turbulence models especially in connection with impingement flows. This work is a preliminary study for future research, where it will be validated and compared with an experimental study on an identical test case.

Therefore, RANS simulations and LES are conducted for an in-row arrangement of nine impinging jets in cross-flow. The study is carried out at the *German Aerospace Center* (DLR) using the in-house *computational fluid dynamics* (CFD) solver *TRACE* (Turbomachinery Research Aerodynamic Computational Environment). The work of this thesis consists of the following aspects:

- **Physical background**: Fundamentals of fluid mechanics and physical phenomena specifically relating to impingement flows.
- **Computational methods**: Review of the computational methods to predict these phenomena as well as various approaches to turbulence modelling.
- **Test case and numerical setup**: Detailed description of the investigated test case and numerical setup.
- **RANS simulation**: RANS simulation of the considered test case with a focus on convergence, grid convergence and heat transfer as well as a sensitivity study.

- **Large eddy simulation**: LES of the considered test case with a focus on grid resolution suitability, statistical convergence and heat transfer as well as a comparison with the RANS study and literature correlations.
- **Conclusion**: Conclusions drawn from the RANS and LES studies and recommendations for further research.

2 Physical Background

The following chapter is divided into three main parts: The governing equations of fluid mechanics as well as the important physical phenomena and flow characteristics of impinging jets. In the first part, the governing equations are presented as a mathematical approach to describe fluid flow. Further information on major physical phenomena such as heat transfer and turbulence is given in the second part. This is essential for understanding the underlying flow characteristics of jet impingement, which are discussed in the third part.

2.1 Governing Equations of Fluid Mechanics

The governing equations of fluid mechanics are crucial for the description of fluid flow. Taking the continuum hypothesis into account, they can be derived from the following three conservation principles:

1. **Conservation of mass**: The rate of change of the mass of a body equals the difference of mass inflow and mass outflow (continuity principle).
2. **Conservation of momentum**: The rate of change of the momentum of a body equals the force applied on this body.
3. **Conservation of energy**: The rate of change of the total energy of a body equals the power of the external forces and the rate at which heat is transferred to this body.

Usually the continuity and momentum equations are also referred to as the *Navier-Stokes equations*. In differential form, the compressible equations can be written as follows.

$$\frac{\partial \rho}{\partial t} + \frac{\partial}{\partial x_i}(\rho u_i) = 0 \tag{2.1}$$

$$\frac{\partial}{\partial t}(\rho u_i) + \frac{\partial}{\partial x_j}(\rho u_j u_i) = -\frac{\partial p}{\partial x_i} + \frac{\partial \tau_{ji}}{\partial x_j} \tag{2.2}$$

$$\frac{\partial}{\partial t}\left[\rho\left(e+\frac{u_i u_i}{2}\right)\right]+\frac{\partial}{\partial x_j}\left[\rho u_j\left(h+\frac{u_i u_i}{2}\right)\right]=\frac{\partial}{\partial x_j}(u_i\tau_{ij})-\frac{\partial q_j}{\partial x_j} \tag{2.3}$$

Body forces can be neglected for the type of flow considered in this work and therefore are not taken into account in Equations 2.2 and 2.3. According to Einstein's summation convention [12], indices that appear twice within an expression have to be summed. For Newtonian fluids [14], the viscous stress tensor τ_{ij} is defined as

$$\tau_{ij}=2\mu S_{ij}-\frac{2}{3}\mu\delta_{ij}\frac{\partial u_k}{\partial x_k} \tag{2.4}$$

with the dynamic viscosity μ and the rate of strain tensor S_{ij}.

$$S_{ij}=\frac{1}{2}\left(\frac{\partial u_i}{\partial x_j}+\frac{\partial u_j}{\partial x_i}\right) \tag{2.5}$$

The heat flux vector q_i can be expressed by using Fourier's law.

$$q_j=-\lambda\frac{\partial T}{\partial x_j} \tag{2.6}$$

There are different models available that form a relation between the pressure p, the density ρ and the temperature T. One of them is the ideal gas model. However, this model is not necessarily applied with the Navier-Stokes equations, so it is presented later in Section 4.2.3. Since the specific enthalpy h also will be mentioned later, a relation to the specific internal energy e is given by following equation.[14, 38, 42]

$$h=e+\frac{p}{\rho} \tag{2.7}$$

2.2 Major Physical Phenomena of Jet Impingement

As fluid flow is described in a rather general context above, this section specifically focuses on physical phenomena regarding jet impingement. The fundamentals of heat transfer are discussed first, since heat transfer characteristics of impinging jets are particularly interesting for engineering applications. The turbulence phenomenon is then introduced as a major influencing factor.

2.2.1 Heat Transfer

There are three types of heat transfer: *Conduction*, *convection* and *radiation*. Heat conduction (or heat diffusion) occurs in the presence of temperature gradients and is described by Fourier's law (see equation 2.6). Heat convection, on the other hand, is a more complex phenomenon and only takes place when a fluid is in motion. A distinction is made between *free* (or *natural*) *convection* and *forced convection*. In the case of free convection, the flow is induced by buoyancy forces due to density differences, whereas in forced convection, the flow is caused by external forces.[27] Radiation is not discussed in this work, as its effects on heat transfer are negligible when dealing with impinging jets. Two important non-dimensional quantities are considered in this work in connection with heat transfer and fluid flow: The Nusselt number and the Prandtl number. The Nusselt number Nu can be interpreted as the ratio between convection and conduction heat transfer.

$$Nu = \frac{\alpha l_c}{\lambda} \tag{2.8}$$

The Prandtl number Pr represents the ratio between momentum diffusivity and thermal diffusivity.[27]

$$Pr = \frac{c_p \mu}{\lambda} \tag{2.9}$$

2.2.2 Turbulence

The majority of flows encountered in engineering applications are turbulent. Turbulence has got a significant effect on heat transfer, thus making its prediction more complex. In References [14, 38], the phenomenon is described as follows.

- Unsteady, appearing 'chaotic'
- Three-dimensional
- Containing vortices/eddies
- Diffusive
- Dissipative
- Consisting of a broad range of length and time scales

The most important non-dimensional quantity relating to turbulence is the Reynolds number Re, which represents the ratio of the inertial to the viscous forces with a characteristic length l_c.

$$Re = \frac{\rho u l_c}{\mu} = \frac{u l_c}{\nu} \tag{2.10}$$

A flow is considered as *laminar flow*, if the Reynolds number is below a critical Reynolds number. Exceeding this critical Reynolds number causes a transition from laminar to *turbulent flow*. The value of the critical Reynolds number depends on the considered flow problem.[38]

It is important to introduce the *energy cascade*, which will be mentioned later in Sections 3.3 and 6.2.4. It represents the energy transfer from the large to the small turbulent scales and can be visualized by the *energy spectrum* as presented in Figure 2.1. The energy spectrum describes the energy E as a function of the wave number k, which serves as an indicator for the size of an eddy. Large eddies have small wave numbers, whereas small eddies have large wave numbers. The energy spectrum is divided into three sections: The *energy containing range*, the *inertial sub-range* and the *dissipation range*.[8, 15]

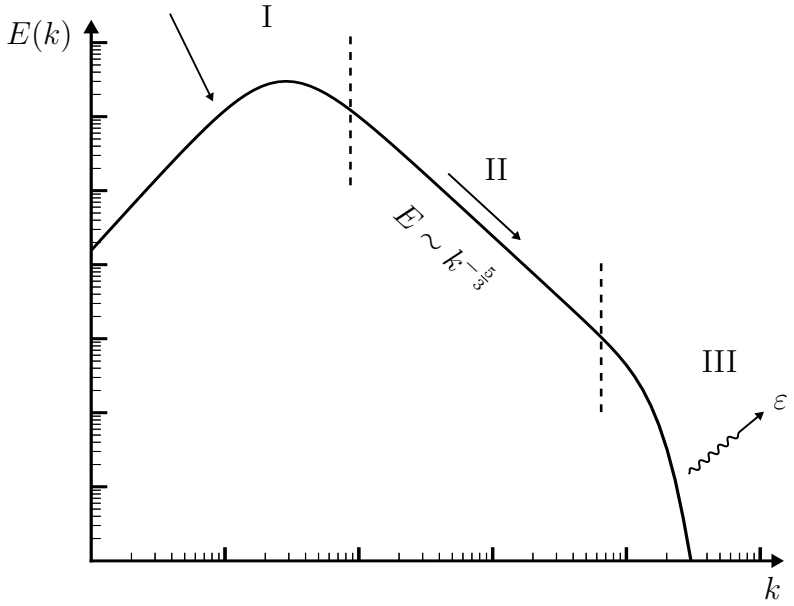

Figure 2.1: Energy spectrum $E(k)$ plotted in a double logarithmic reference frame

I) **Energy containing range**: This range contains the largest eddies, which extract energy from the mean flow and carry most of the energy in the spectrum.

II) **Inertial sub-range**: In this range, the energy is transferred from the energy containing range (I) to the dissipation range (III) with the Energy E being proportional to $k^{-\frac{5}{3}}$. The inertial sub-range only exists under the condition of fully developed turbulence and increases with higher Reynolds numbers.

III) **Dissipation range**: This range contains the small and isotropic eddies. The kinetic energy of these eddies is transformed into internal energy, also referred to as dissipation.

While the largest scales correspond to the considered flow geometry (such as the boundary layer thickness), the smallest possible scales are defined by the *Kolmogorov scales*. They are determined by the kinematic viscosity ν and the dissipation rate ε.[8]

$$\text{Length scale } l_\eta = \left(\frac{\nu^3}{\varepsilon}\right)^{\frac{1}{4}} \tag{2.11}$$

$$\text{Time scale } t_\eta = \left(\frac{\nu}{\varepsilon}\right)^{\frac{1}{2}} \tag{2.12}$$

$$\text{Velocity scale } u_\eta = (\nu\varepsilon)^{\frac{1}{4}} \tag{2.13}$$

2.3 Flow Characteristics of Impinging Jets

This section specifically focusses on the flow behaviour of impinging jets. The flow regions and their respective flow mechanisms are presented first. In order to illustrate the advantages of jet impingement, the underlying heat transfer characteristics and their contributing factors are discussed afterwards.

Impinging jets are divided into four major flow regimes (see Figure 2.2): The *free jet region*, the *stagnation region*, the *wall jet region* and the *fountain flow region*.

I) **Free jet region**: The free jet evolves at the nozzle outlet and consists of a *potential core* and a *shear layer*. The potential core is a region in the center of the free jet where velocity remains constant. In downstream direction it is increasingly displaced by the shear layer until it vanishes at a certain point. This shear layer develops due to the velocity gradient between the free jet and the ambient fluid. The spreading of the shear layer is caused by Kelvin-Helmholtz instability and roll-up of vortices. As the potential core disappears, the flow is fully developed and the velocity profile forms a Gaussian distribution.[10, 21]

II) **Stagnation region**: As the jet reaches the target plate, its axial velocity drops rapidly, causing the pressure to rise to a maximum. The target plate deflects the stream from an axial to a radial direction of flow.[21]

III) **Wall jet region**: In the wall jet region, the fluid flows parallel to the target plate. Two distinct shear layers are formed, since the flow is influenced by the wall as well as by the ambient fluid.[10]

IV) **Fountain flow region**: This flow region only exists for confined or multiple impinging jets. Fountain flow and recirculation may occur, caused by interactions with side walls and adjacent jets.[23, 28]

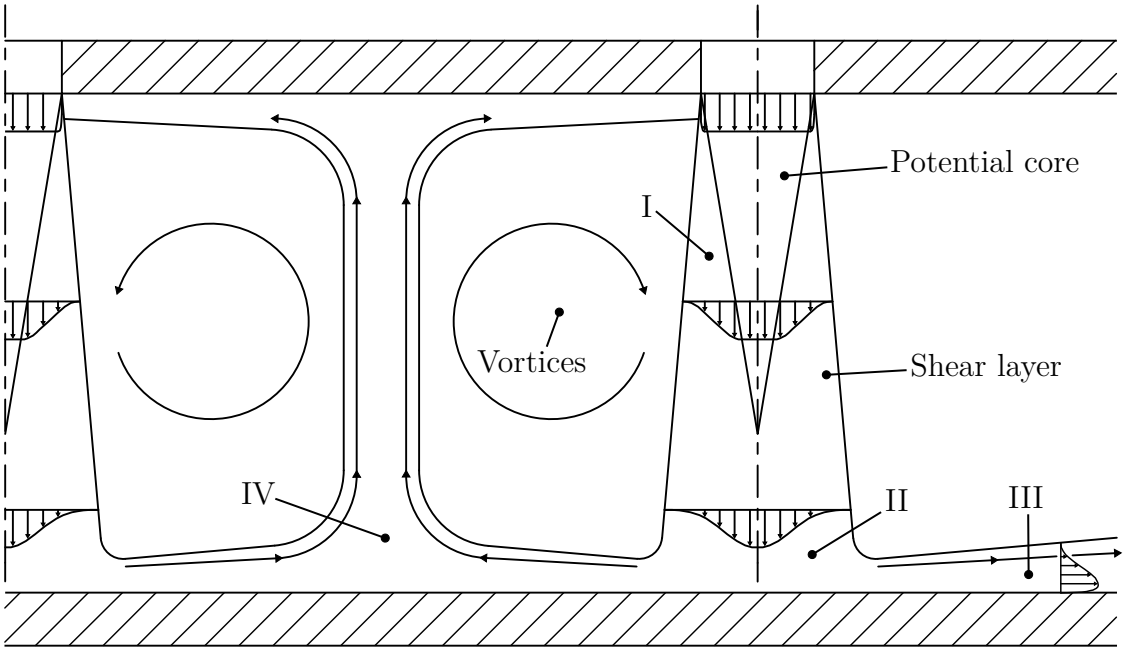

Figure 2.2: Flow regions of an impinging jet in a multi-jet configuration

As for most convection cooling mechanisms, the heat transfer of impinging jets is mainly caused by forced convection. However, it is up to three times higher for impingement cooling than for conventional convection cooling at a given maximum flow speed. This is due to the following three reasons. First of all, the boundary layer (viscous as well as thermal) is thinner for impinging jets. Secondly, and as mentioned above, the wall jet forms two distinct shear layers leading to further increase in turbulence level and thus heat transfer. And thirdly, the fluid that already has impinged the target plate causes additional turbulence in the surrounding fluid.[9, 44]

There are numerous physical and geometrical factors that contribute to the heat transfer of impinging jet flows. The most important physical factors are expressed by the non-dimensional quantities Re, Pr and the Mach number Ma. Ma is defined by the flow velocity u and the speed of sound a, which is computed using the heat capacity ratio κ, the gas constant R and the temperature T [32].

$$Ma = \frac{u}{a} = \frac{u}{\sqrt{\kappa R T}} \tag{2.14}$$

They provide a basis for the comparison of different impinging jet arrangements and can be used for empirical heat transfer calculations based on correlations from the literature. Following geometrical parameters have an additional influence on heat transfer [44]:

- Nozzle height H

- Radial distance between measuring point and stagnation point
- Axial distance (or height) between measuring point and target plate
- Nozzle-to-nozzle spacing s_{nozzle}
- Area of nozzle cross-section
- Area of target plate

3 Computational Methods

This chapter focusses on the fundamentals of CFD. First, an introduction to this major topic is given by presenting the basic idea together with the discretization methods. As the flows considered in this work are turbulent, three different approaches to the simulation of turbulence are presented thereafter: DNS, statistical turbulence modelling and LES.

Since the Navier-Stokes equations (see Section 2.1) can only be solved for specific and mostly simplified flow problems, alternative approaches have to be taken to deal with other types of fluid flow: With CFD, the Navier-Stokes equations can be solved numerically on a computer. This method is particularly interesting for engineering practice, since it is flexible and allows application for rather complex flow conditions.[14]

First of all, a *discretization method* is used to approximate differential equations (in this case the Navier-Stokes equations) by a system of difference equations, which can later be solved numerically. The most important approaches are the finite difference, finite element and finite volume method. However, the finite volume method is most commonly used in CFD and is also adapted in this study. For spatial discretization, a *numerical grid* has to be generated. It consists of numerous cells, on which the conservation principles are applied by solving the underlying equations. As visualized in Figure 3.1, there are structured, unstructured and block-structured grids.[14, 36]

Structured grids consist of rectangles (two dimensions) or hexahedrons (three dimensions). The grid lines are arranged in such a way that members of the same index do not cross each other and cross each member of the other index only once. As a result, every cell can be assigned with a distinct and consecutive index. However, structured grids are not as flexible as unstructured grids, which is why they cannot be applied to complex geometries.[14]

By definition, *unstructured grids* consist of rather arbitrary shapes, although in practice, they usually are limited to triangles/tetrahedrons and rectangles/hexahedrons. In contrast to structured grids, unstructured grids are more flexible regarding the adaptation to complex geometries. However, memory consumption and computation time typically are higher, since their cells are not indexed consecutively.[14]

On the coarse level, *block-structured grids* are divided into unstructured cells, which themselves are subdivided into structured cells on the fine level. As a consequence, the advantages of both structured and unstructured grids are combined.[14]

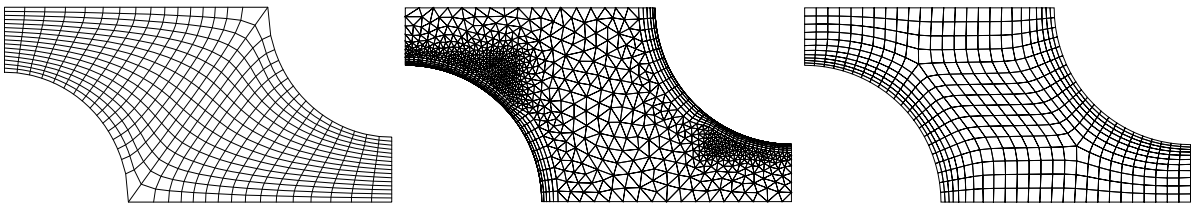

Structured grid Unstructured grid Block-structured grid

Figure 3.1: Two-dimensional example of three grid types: Structured, unstructured and block-structured grids

As the prediction of turbulent flows is complicated even with the help of CFD, several approaches have been made to modify the Navier-Stokes equations in such a way that their approximation is less time- and memory-consuming. These approaches are discussed in the following sections, since they are essential for the research focus of this work.

3.1 Direct Numerical Simulation

As its name suggests, the *direct numerical simulation* (DNS) approximates the Navier-Stokes equations directly. Neither averaging nor modelling is used with this method, which is why the entire energy spectrum has to be computed (see Figure 2.1). It is an absolute requirement that the computation domain is at least as large as the considered flow domain (or the largest eddy) and that the Kolmogorov scales are resolved spatially and temporally. DNS always implies high computational efforts, thus making it only applicable for simple geometries and low Reynolds number flows. Typically, these efforts are not reasonable for engineering applications. However, there is a scientific interest in studying the turbulence phenomenon with DNS.[14]

3.2 Statistical Turbulence Modelling

In contrast to DNS, *statistical turbulence modelling* implies that a turbulence model is applied to the entire range of turbulent scales. The Navier-Stokes equations are averaged, assuming that every flow variable ϕ can be decomposed into an averaged component $\bar{\phi}$

and a fluctuating component ϕ' (see Figure 3.2).

$$\phi = \bar{\phi} + \phi' \tag{3.1}$$

The idea behind this approach is that the averaged component of a flow variable usually is most interesting for engineering research.[4]

According to Reynolds [33], the time-averaged component can be written as follows.

$$\bar{\phi} = \lim_{\Delta t \to \infty} \frac{1}{\Delta t} \int_{t_0}^{t_0+\Delta t} \phi dt \tag{3.2}$$

Applied to the Navier-Stokes equations, this averaging procedure leads to the RANS equations. Unfortunately, they are only suitable for incompressible flows, which is why another approach has to be taken when compressible flows are considered.[4]

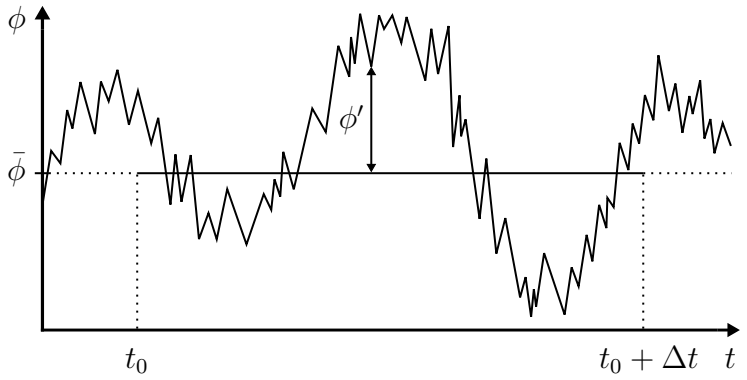

Figure 3.2: Visualization of the time-averaged and the fluctuating component of a flow variable together with the integration limits

This approach, also known as *Favre-averaging* [13], is based on the density weighted decomposition of a flow variable with the Favre-averaged component $\tilde{\phi}$ and the fluctuating component ϕ''. It should be noted that statistical turbulence modelling techniques often are referred to as RANS, although the underlying equations may be Favre-averaged.

$$\phi = \tilde{\phi} + \phi'' \tag{3.3}$$

The Favre-averaged component of a flow variable can be written as follows.[4]

$$\tilde{\phi} = \frac{1}{\bar{\rho}} \lim_{\Delta t \to \infty} \frac{1}{\Delta t} \int_{t_0}^{t_0+\Delta t} \rho\phi dt = \frac{1}{\bar{\rho}} \overline{\rho\phi} \tag{3.4}$$

For this approach, the density ρ and the pressure p most commonly are Reynolds-

averaged, while the remaining flow variables are Favre-averaged. By applying this averaging procedure to the Navier-Stokes equations, the *Favre-averaged Navier-Stokes* equations are obtained. These equations (continuity, momentum and energy equation) are mentioned below, as they are essential for the computation of the compressible flows considered in this work.

$$\frac{\partial \bar{\rho}}{\partial t} + \frac{\partial}{\partial x_i}(\bar{\rho}\tilde{u}_i) = 0 \tag{3.5}$$

$$\frac{\partial}{\partial t}(\bar{\rho}\tilde{u}_i) + \frac{\partial}{\partial x_j}(\bar{\rho}\tilde{u}_j\tilde{u}_i) = -\frac{\partial \bar{p}}{\partial x_i} + \frac{\partial}{\partial x_j}\left(\tilde{\tau}_{ij} - \bar{\rho}\widetilde{u_i'' u_j''}\right) \tag{3.6}$$

$$\begin{aligned}\frac{\partial}{\partial t}\left[\bar{\rho}\left(\tilde{e} + \frac{\tilde{u}_i\tilde{u}_i}{2} + \frac{\widetilde{u_i'' u_i''}}{2}\right)\right] + \frac{\partial}{\partial x_j}\left[\tilde{u}_j\bar{\rho}\left(\tilde{h} + \frac{\tilde{u}_i\tilde{u}_i}{2} + \frac{\widetilde{u_i'' u_i''}}{2}\right)\right] \\ = \frac{\partial}{\partial x_j}\left[-\tilde{q}_j - \bar{\rho}\widetilde{u_j'' h''} + \widetilde{\tau_{ij} u_i''} - \bar{\rho}\widetilde{u_j'' k}\right] \\ + \frac{\partial}{\partial x_j}\left[\tilde{u}_i\left(\tilde{\tau}_{ij} - \bar{\rho}\widetilde{u_i'' u_j''}\right)\right]\end{aligned} \tag{3.7}$$

Similarly to equation 2.6, Fourier's law describes the Favre-averaged specific heat flux $\tilde{q}_j$.

$$\tilde{q}_j = -\lambda\frac{\partial \tilde{T}}{\partial x_j} \tag{3.8}$$

The following term is defined as the Favre-averaged *specific Reynolds stress tensor* τ_{ij}^F.

$$\tau_{ij}^F = -\widetilde{u_i'' u_j''} \tag{3.9}$$

The Favre-averaged *specific turbulent kinetic energy* $\tilde{k}$ is obtained by taking the trace of the specific Reynolds stress tensor.

$$\tilde{k} = \frac{1}{2}\widetilde{u_i'' u_i''} \tag{3.10}$$

The Reynolds stress tensor as well as the turbulent kinetic energy are crucial for the description of turbulent flows. However, the Reynolds stress tensor itself has to be modelled, since it is an unknown term of the Favre-averaged Navier-Stokes equations. There are numerous approaches described in the literature to model the Reynolds stress tensor. The turbulence model used later for this study is the shear stress transport k-ω model by Menter [31]. As it is based on the k-ε and k-ω model, these two models are discussed first.[4, 42]

3.2.1 Standard k-ε Model

The k-ε model is a two-equation model. It is based on the *eddy viscosity hypothesis* proposed by Boussinesq [5], which states that there is a linear mathematical relation between the Reynolds stress $\bar{\rho}\tau_{ij}^F$ and the rate of strain $\tilde{S}_{ij}$, similar to the dynamic (or molecular) viscosity μ. This relation is introduced as the eddy viscosity μ_T.

$$\bar{\rho}\tau_{ij}^F = 2\mu_T\tilde{S}_{ij} - \frac{2}{3}\mu_T\delta_{ij}\frac{\partial\tilde{u}_k}{\partial x_k} - \frac{2}{3}\bar{\rho}k\delta_{ij} \tag{3.11}$$

While the molecular viscosity is a major property of a fluid, the eddy viscosity is a function of the convective mechanisms in a turbulent flow field. Equation 3.11 contains two unknown variables: The specific turbulent kinetic energy k, often simply referred to as the turbulent kinetic energy, and the eddy viscosity μ_T. Following relation for the eddy viscosity is obtained from dimension analysis. It includes the model constant C_μ.[2, 4, 42]

$$\mu_T = C_\mu\rho\frac{k^2}{\varepsilon} \tag{3.12}$$

The actual k-ε model applies to the transport equations of k (equation 3.13) and ε (equation 3.14), which are derived from the transport equation for the specific Reynolds stress τ_{ij}^F (the equation is given in [42]). These equations typically consist of the total time derivative of the respective flow variable as well as a diffusion, a production and a dissipation term.

$$\frac{\partial}{\partial t}(\rho k) + \frac{\partial}{\partial x_i}(\rho k u_i) = \frac{\partial}{\partial x_j}\left[\left(\mu + \frac{\mu_T}{\sigma_k}\right)\frac{\partial k}{\partial x_j}\right] + 2\mu_T S_{ij}S_{ij} - \rho\varepsilon - 2\rho\varepsilon Ma_T^2 + S_k \tag{3.13}$$

$$\frac{\partial}{\partial t}(\rho\varepsilon) + \frac{\partial}{\partial x_i}(\rho\varepsilon u_i) = \frac{\partial}{\partial x_j}\left[\left(\mu + \frac{\mu_T}{\sigma_\varepsilon}\right)\frac{\partial\varepsilon}{\partial x_j}\right] + C_{1\varepsilon}\frac{\varepsilon}{k}(2\mu_T S_{ij}S_{ij}) - C_{2\varepsilon}\rho\frac{\varepsilon^2}{k} + S_\varepsilon \tag{3.14}$$

S_k and S_ε are source terms, which have to be defined prior to the simulation. The turbulent Mach number Ma_T is defined by the turbulent kinetic energy k and the speed of sound a.

$$Ma_T = \sqrt{\frac{2k}{a^2}} \tag{3.15}$$

According to the Launder-Sharma model, the model coefficients $C_{1\varepsilon}$, $C_{2\varepsilon}$, C_μ, σ_k and σ_ε can be set as follows.

$$C_{1\varepsilon} = 1.44,\ C_{2\varepsilon} = 1.92,\ C_\mu = 0.09,\ \sigma_k = 1.0,\ \sigma_\varepsilon = 1.3 \tag{3.16}$$

Damping functions are introduced for low Reynolds number k-ε-models in order to accurately predict flows in the near-wall region. Further details about the k-ε model are given in Reference [2].

3.2.2 Wilcox k-ω Model

The *k-ω model* proposed by Wilcox [42] is also based on the eddy viscosity hypothesis. However, a different relation for the eddy viscosity is used for this model. A new variable is introduced, referred to as the specific dissipation rate ω. α^* and β^* represent model coefficients.

$$\mu_T = \alpha^* \rho \frac{k}{\omega} \tag{3.17}$$

$$\omega = \frac{\varepsilon}{\beta^* k} \tag{3.18}$$

Consequently, the k-ω model models the transport equations for the turbulent kinetic energy k (equation 3.19) and the specific dissipation rate ω (equation 3.20).

$$\frac{\partial}{\partial t}(\rho k) + \frac{\partial}{\partial x_i}(\rho k u_i) = \frac{\partial}{\partial x_j}\left[\left(\mu + \frac{\mu_T}{\sigma_k}\right)\frac{\partial k}{\partial x_j}\right] + 2\mu_T S_{ij} S_{ij} - Y_k + S_k \tag{3.19}$$

$$\frac{\partial}{\partial t}(\rho \omega) + \frac{\partial}{\partial x_i}(\rho \omega u_i) = \frac{\partial}{\partial x_j}\left[\left(\mu + \frac{\mu_T}{\sigma_\omega}\right)\frac{\partial \omega}{\partial x_j}\right] + 2\alpha\frac{\omega}{k}\mu_T S_{ij} S_{ij} - Y_\omega + S_\omega \tag{3.20}$$

The dissipation terms Y_k and Y_ω as well as the model coefficient α are defined in Appendix A.1. As with the k-ε model, S_k and S_ω are predefined source terms. The closure coefficients are set as follows.

$$\begin{gathered} \alpha_\infty^* = 1,\ \alpha_\infty = 0.52,\ \alpha_0 = \frac{1}{9},\ \beta_\infty^* = 0.09,\ \beta_i = 0.072,\ R_\beta = 8 \\ R_k = 6,\ R_\omega = 2.95,\ \zeta^* = 1.5,\ Ma_{T0} = 0.25,\ \sigma_k = 2.0,\ \sigma_\omega = 2.0 \end{gathered} \tag{3.21}$$

Further information on the k-ω model can be found in [2].

3.2.3 Shear Stress Transport k-ω Model

The *shear stress transport (SST) k-ω model* proposed by Menter [31] represents a combination of the k-ε and the k-ω model. It is motivated by the different advantages and disadvantages that relate to each of these two models. The k-ω model shows high accuracy in the near-wall region without the need of any damping functions, which increases its

numerical stability. Additionally, it is superior to the k-ε model in adverse pressure flows. However, the k-ω model is highly dependent upon the free stream value of ω, which makes it less suitable for wake regions. Free shear layers are also computed more accurately by the k-ε-model. Consequently, the k-ω model is employed in the near-wall region, whereas the k-ε model is employed in the far field. Therefore, the blending function F_1 is designed to switch between the k-ε and k-ω model as required. Another blending function F_2 is introduced to switch between two distinct definitions for the eddy viscosity. The formulation of the k-ε model is transformed into the k-ω formulation, so that only two equations are needed: One for k and one for ω.[2, 4, 31]

For this model, the eddy viscosity μ_T can be obtained from the following equation:

$$\mu_T = \rho \frac{k}{\omega} \frac{1}{\max\left[\frac{1}{\alpha^*}, \frac{\sqrt{2S_{ij}S_{ij}}F_2}{a_1\omega}\right]} \tag{3.22}$$

The model coefficient α^* and the blending function F_2 are given in Appendix A.2. With the k-ω SST model, the modelled transport equations for the turbulent kinetic energy k (equation 3.23) and the specific dissipation rate ω (equation 3.24) are quite similar to the transport equations of the k-ω model:

$$\frac{\partial}{\partial t}(\rho k) + \frac{\partial}{\partial x_i}(\rho k u_i) = \frac{\partial}{\partial x_j}\left[\left(\mu + \frac{\mu_T}{\sigma_k}\right)\frac{\partial k}{\partial x_j}\right] + 2\mu_T S_{ij}S_{ij} - Y_k + S_k \tag{3.23}$$

$$\frac{\partial}{\partial t}(\rho \omega) + \frac{\partial}{\partial x_i}(\rho \omega u_i) = \frac{\partial}{\partial x_j}\left[\left(\mu + \frac{\mu_T}{\sigma_\omega}\right)\frac{\partial \omega}{\partial x_j}\right] + 2\frac{\alpha}{\nu_T}\mu_T S_{ij}S_{ij} - Y_\omega + D_\omega + S_\omega \tag{3.24}$$

The model coefficients α, σ_k and σ_ω as well as the dissipation terms Y_k and Y_ω are defined in Appendix A.2. As with the k-ε and k-ω model, S_k and S_ω are predefined source terms. D_ω is a cross-diffusion term, which is also given in Appendix A.2. The model constants are defined below.

$$\begin{gathered} \sigma_{k,1} = 1.176,\ \sigma_{\omega,1} = 2.0,\ \sigma_{k,2} = 1.0,\ \sigma_{\omega,2} = 1.168 \\ a_1 = 0.31,\ \beta_{i,1} = 0.075,\ \beta_{i,2} = 0.0828 \end{gathered} \tag{3.25}$$

The remaining constants α^*_∞, α_0, β^*_∞, R_β, R_k, R_ω, ζ^* and Ma_{T0} have already been defined for the k-ω model. The SST k-ω model is further described in [2].

3.3 Large Eddy Simulation

With LES, the large scales are simulated directly, whereas the small scales are modelled. The computation efforts are considerably lower than with DNS, yet the large and most important scales are resolved (see Figure 3.3). As a consequence, the LES can be applied to much higher Reynolds numbers than the DNS. The approach is based on following two circumstances. First of all, small scales are less dependent upon boundary conditions and have only a minor influence on the Reynolds stresses. Secondly, they are nearly isotropic and have almost universal characteristics, which is why their behaviour can be predicted more accurately.[4, 8, 42]

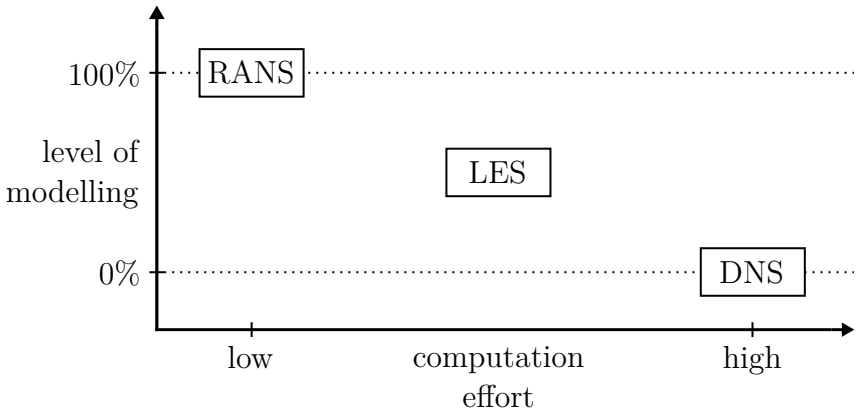

Figure 3.3: Comparison of RANS, LES and DNS with respect to the level of modelling and computation effort

The grid cells of an LES domain act as a filter. Consequently, every flow variable ϕ is divided into a resolved (filtered) part $\hat{\phi}$ and a non-resolved part ϕ'''.

$$\phi = \hat{\phi} + \phi''' \tag{3.26}$$

The filtered component $\hat{\phi}$ can be considered as a quantity that is spatially averaged over a grid cell. The filtering operation is mathematically represented by the convolution product (denoted by $*$), which is applied to the flow variable ϕ with a low pass frequency filter G. Δ_{cut} denotes the respective spatial cut-off scale, which is generally defined as $\Delta_{cut} = (\Delta x \Delta y \Delta z)^{\frac{1}{3}}$ with the respective cell dimensions Δx, Δy and Δz.

$$\hat{\phi}(x,t) = G * \phi(\xi,t') = \frac{1}{\Delta_{cut}} \int_{-\infty}^{\infty} \int_{-\infty}^{\infty} G\left(\frac{x-\xi}{\Delta_{cut}}, t-t'\right) \phi(\xi,t') dt' d^3\xi \tag{3.27}$$

There are different filter functions available, such as the top hat (or box), cut-off and

Gaussian filter. However, the top hat filter (see Figure 3.4a) is used in this work. The cut-off limit is employed in the inertial sub-range (see Figure 3.4b).

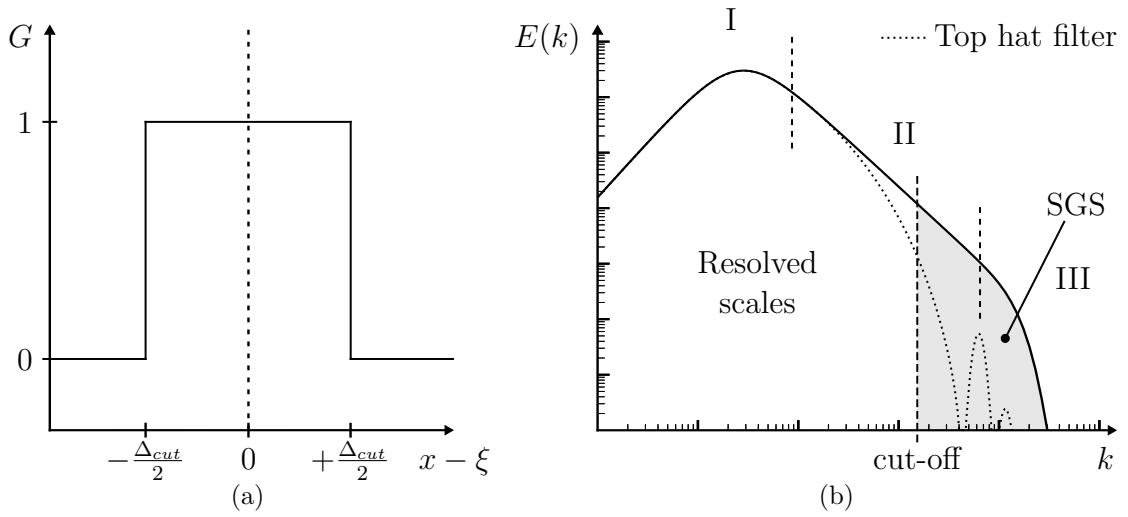

Figure 3.4: Top hat filter function in physical space (a) and energy spectrum with cut-off limit and top hat filter (b)

It should be noted that the top hat filter is sharp in physical space, but not in frequency (or wave number) space. Its filter function for physical space can be written as follows.[4, 8, 15, 20]

$$G(x-\xi) = \begin{cases} \frac{1}{\Delta_{cut}} & \text{if } |x-\xi| \leq \frac{\Delta_{cut}}{2} \\ 0 & \text{otherwise} \end{cases} \tag{3.28}$$

Since the decomposition procedure from equation 3.26 is only suitable for incompressible flows, density weighted *Favre-filtering* has to be introduced for compressible flows. Every flow variable ϕ is divided into a Favre-filtered component $\tilde{\hat{\phi}}$ and a fluctuating component based on Favre-filtering ϕ''''.

$$\phi = \tilde{\hat{\phi}} + \phi'''' \tag{3.29}$$

The Favre-filtered component $\tilde{\hat{\phi}}$ is defined by following equation.

$$\tilde{\hat{\phi}} = \frac{1}{\hat{\rho}}\widehat{\rho\phi} \tag{3.30}$$

The *Favre-filtered Navier-Stokes equations* (continuity, momentum and energy equation) are obtained by applying the Favre-filtering procedure to the Navier-Stokes equations. The following equations are written in such a way that the right-hand side only consists

of subgrid-terms.

$$\frac{\partial \hat{\rho}}{\partial t} + \frac{\partial}{\partial x_j}\left(\hat{\rho}\tilde{\hat{u}}_j\right) = 0 \tag{3.31}$$

$$\frac{\partial}{\partial t}\left(\hat{\rho}\tilde{\hat{u}}_i\right) + \frac{\partial}{\partial x_j}\left(\hat{\rho}\tilde{\hat{u}}_i\tilde{\hat{u}}_j\right) + \frac{\partial \hat{p}}{\partial x_i} - \frac{\partial \breve{\tau}_{ij}}{\partial x_j} = -\frac{\partial}{\partial x_j}\left(\hat{\rho}\tau_{ij}^T\right) + \frac{\partial}{\partial x_j}\left(\hat{\tau}_{ij} - \breve{\tau}_{ij}\right) \tag{3.32}$$

$$\frac{\partial \breve{e}}{\partial t} + \frac{\partial}{\partial x_j}\left(\left(\breve{e} + \hat{p}\right)\tilde{\hat{u}}_j\right) - \frac{\partial}{\partial x_j}\left(\breve{\tau}_{ij}\tilde{\hat{u}}_i\right) + \frac{\partial \breve{q}_j}{\partial x_j} = -\alpha_1 - \alpha_2 - \alpha_3 + \alpha_4 + \alpha_5 + \alpha_6 \tag{3.33}$$

τ_{ij}^T denotes the *turbulent stress tensor* and $\breve{\tau}_{ij}$, $\breve{e}$ and $\breve{q}$ are functions of filtered variables.

$$\tau_{ij}^T = \widetilde{\widehat{u_i u_j}} - \tilde{\hat{u}}_i\tilde{\hat{u}}_j \tag{3.34}$$

The subgrid-terms α_i from the energy equation are defined as follows.

$$\alpha_1 = \tilde{\hat{u}}_i \frac{\partial}{\partial x_j}\left(\hat{\rho}\tau_{ij}^T\right) \tag{3.35}$$

$$\alpha_2 = \left(\frac{1}{\kappa - 1}\right)\frac{\partial}{\partial x_j}\left(\widehat{pu_j} - \hat{p}\tilde{\hat{u}}_j\right) \tag{3.36}$$

$$\alpha_3 = \widehat{\left(p\frac{\partial u_j}{\partial x_j}\right)} - \hat{p}\frac{\partial \tilde{\hat{u}}_j}{\partial x_j} \tag{3.37}$$

$$\alpha_4 = \widehat{\left(\tau_{ij}\frac{\partial u_j}{\partial x_j}\right)} - \hat{\tau}_{ij}\frac{\partial \tilde{\hat{u}}_i}{\partial x_j} \tag{3.38}$$

$$\alpha_5 = \frac{\partial}{\partial x_j}\left(\hat{\tau}_{ij}\tilde{\hat{u}}_i - \breve{\tau}_{ij}\tilde{\hat{u}}_i\right) \tag{3.39}$$

$$\alpha_6 = \frac{\partial}{\partial x_j}\left(\hat{q}_j - \breve{q}_j\right) \tag{3.40}$$

The heat capacity ratio is represented by κ.[20, 39]

$$\kappa = \frac{c_p}{c_v} \tag{3.41}$$

The subgrid-terms are not resolved by the grid and hence have to be modelled by a subgrid scale (SGS) model. However, the subgrid-terms of the energy equation are neglected for compressible flows at low Mach numbers so that modelling the deviatoric part of the turbulent stress tensor $\tau_{ij}^{T,d}$ is presumed to be sufficient. Usually, the isotropic part τ_{kk}^T is not modelled, but included in the filtered pressure instead.

$$\tau_{ij}^{T,d} = \tau_{ij}^T - \frac{1}{3}\delta_{ij}\tau_{kk}^T \tag{3.42}$$

There are many approaches available to model the deviatoric part of the turbulent stress tensor, but the model used in this work is the Wall-Adapting Local Eddy-viscosity (WALE) model [11]. As it is based on the Smagorinsky model, this model will be discussed first.[2, 20, 39]

3.3.1 Smagorinsky Model

The *Smagorinsky model* [37] is based on the eddy viscosity hypothesis proposed by Boussinesq [5] (see Section 3.2.1). Therefore, the subgrid viscosity ν_{sgs} is introduced to model the deviatoric part of the turbulent stress tensor $\tau_{ij}^{T,d}$.

$$\tau_{ij}^{T,d} = -2\nu_{sgs}\left(\tilde{\hat{S}}_{ij} - \frac{1}{3}\delta_{ij}\tilde{\hat{S}}_{kk}\right) \tag{3.43}$$

By means of dimension analysis, following relation for the subgrid viscosity ν_{sgs} is obtained with a characteristic length l_c and a characteristic time t_c.

$$\nu_{sgs} = \frac{l_c^2}{t_c} \tag{3.44}$$

According to Smagorinsky, the time scale can be derived from the resolved strain rate tensor $|\hat{S}|$, while the length scale is derived from the Smagorinsky constant C_s and the spatial cut-off scale Δ_{cut}. Typically, C_s is set to a value ranging from 0.1 to 0.2.

$$\nu_{sgs} = C_s^2\Delta_{cut}^2|\tilde{\hat{S}}| \tag{3.45}$$

The resolved strain rate tensor $|\hat{S}|$ is defined by following equation.

$$|\tilde{\hat{S}}| = \sqrt{2\tilde{\hat{S}}_{ij}\tilde{\hat{S}}_{ij}} \tag{3.46}$$

Several values for the Smagorinsky constant are given in the literature. Unfortunately, the Smagorinsky model does not provide proper damping of turbulent fluctuations and therefore eddy viscosity in near-wall regions. As a consequence, another approach has to be taken to deal with flow problems that include walls.[2, 20]

3.3.2 WALE Model

The *WALE model* proposed by Ducros et al. [11] is an eddy viscosity model that considers the dampening effect of molecular viscosity on turbulent fluctuations in the near-wall region. This approach, however, does not make use of damping functions, but is based on spatial velocity gradients instead. Consequently, model complexity is kept on a relatively low level, since wall distance and skin friction are not required as input parameters.[20]

Similarly to the Smagorinsky Model, the length scale is obtained from a model constant C_w and the spatial cut-off scale Δ_{cut}. However, the determination of the time scale functions differently. A new operator S_{ij}^d based on the gradient velocity tensor $\tilde{\hat{g}}_{ij} = \frac{\partial u_i}{\partial x_j}$ is introduced.

$$S_{ij}^d = \frac{1}{2}\left(\tilde{\hat{g}}_{ij}^2 + \tilde{\hat{g}}_{ji}^2\right) - \frac{1}{3}\delta_{ij}\tilde{\hat{g}}_{kk}^2 \tag{3.47}$$

For the WALE model, the time scale is defined by S_{ij}^d and the Favre-filtered rate of strain tensor $\tilde{\hat{S}}_{ij}$. As a result, following formulation for the subgrid viscosity is obtained.

$$\nu_{sgs} = C_w^2 \Delta_{cut}^2 \frac{\left(S_{ij}^d S_{ij}^d\right)^{3/2}}{\left(\tilde{\hat{S}}_{ij}\tilde{\hat{S}}_{ij}\right)^{5/2} + \left(S_{ij}^d S_{ij}^d\right)^{5/4}} \tag{3.48}$$

The model constant C_w can be obtained from the Smagorinsky constant C_s by using following expression.[2, 11, 20]

$$C_w \approx \sqrt{10.6} C_s \tag{3.49}$$

4 Test Case and Numerical Setup

In this chapter, the test case and numerical setup considered in this study are introduced. First, an overview of the geometry and basic arrangement of the test case is given. The numerical grids that are used for the RANS and LES studies are presented thereafter. Finally, crucial information about the boundary conditions and gas model is given.

4.1 Test Case

The considered impinging jet configuration is designed to model the impingement cooling mechanisms that are used for turbine blade cooling. The configuration can be described as an in-line arrangement of nine impinging jets in a cross-flow environment (see Figure 4.1).

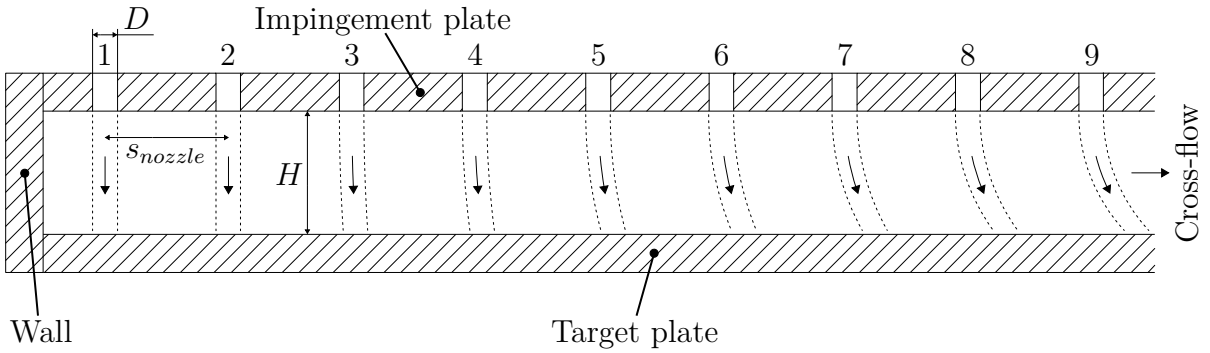

Figure 4.1: Longitudinal section of the considered impinging jet configuration with nine impinging jets in a cross-flow (drawing not in scale)

The impingement plate is equipped with nine circular orifices that are arranged in a straight line. A duct with a quadratic cross-section is formed by the impingement plate, the target plate and two side walls. The cooling air is supplied by a plenum (see Figure 4.2), which is positioned on the upper side of the impingement plate and thus the flow channel. An air suction system draws air through the domain with a constant mass flow $\dot{m}_{target}$ of 0.01998 kg/s. It induces a cross-flow and is located at the downstream end of

the flow channel. A heating plate partly covers the target plate and provides a constant heat flux q_{hp} of 5,000 W/m^2 to model the heat flux caused by the hot gases in a gas turbine. The coordinate origin lies directly below the center of nozzle 7 on the target plate. Figure 4.2 shows a three-dimensional view of the considered test configuration as well as a cross-sectional view of the flow channel.

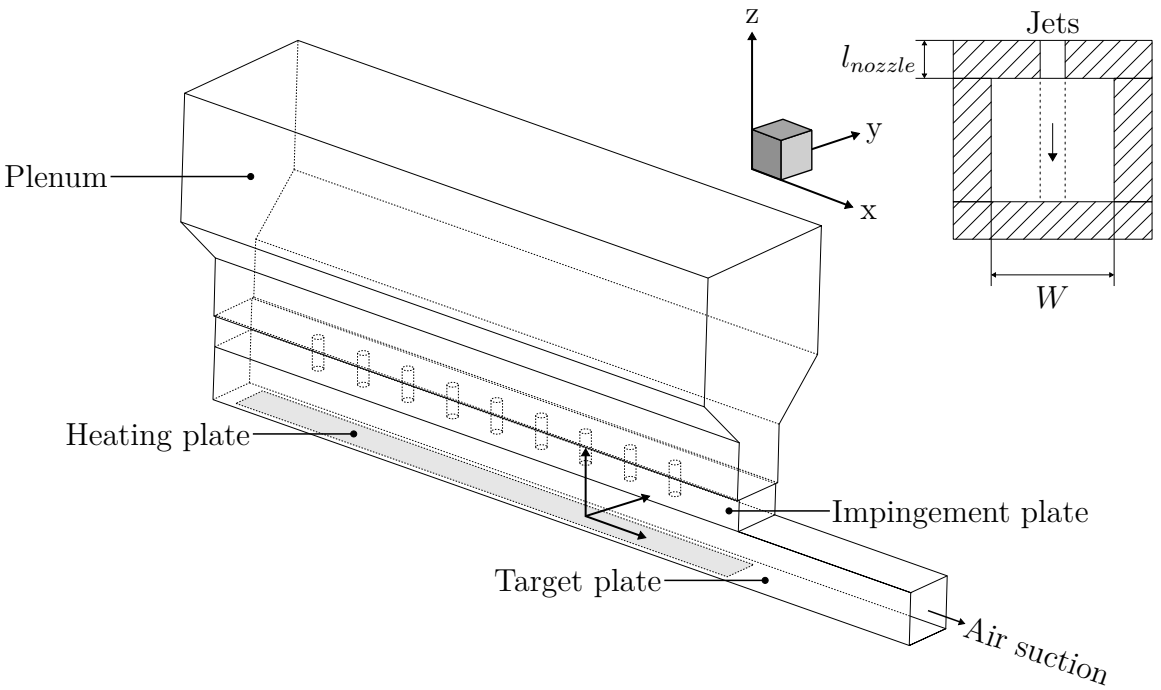

Figure 4.2: Three-dimensional view of the considered impinging jet configuration and cross-sectional view of the flow channel (drawing not in scale)

The most important geometrical parameters of the considered configuration are given in Table 4.3. They allow a direct comparison with other impinging jet in cross-flow cases from the literature (see References [18, 19, 22, 26, 30]). The nozzle diameter D, nozzle height H and nozzle-to-nozzle spacing s_{nozzle} are visualized in Figure 4.1. The channel width W and nozzle length l_{nozzle} are visualized in Figure 4.2.

Table 4.3: Important dimensions of the considered impinging jet configuration

Dimension	Value
Nozzle diameter D	0.0152 m
Nozzle height H	0.076 m (5×D)
Nozzle-to-nozzle spacing s_{nozzle}	0.076 m (5×D)
Specific heat flux (heating plate) q_{hp}	5,000 W/m^2
Channel width W	0.076 m (5×D)

Nozzle length l_{nozzle}	0.0456 m (3×D)

Taking the above mentioned parameters into account, the averaged velocity w_{inlet} and Reynolds number Re_{inlet} at the nozzle inlets can be calculated using following equations. The inlet density ρ_{inlet} and the inlet viscosity μ_{inlet} are obtained from the ideal gas law and the Sutherland model using the inlet pressure p_{inlet} and the inlet temperature T_{inlet} (see Sections 4.2.2 and 4.2.3).

$$w_{inlet} = \frac{4}{9}\frac{\dot{m}_{target}}{\rho_{inlet}\pi D^2} = 10.263 \text{ m/s} \tag{4.1}$$

$$Re_{inlet} = \frac{\rho_{inlet} w_{inlet} D}{\mu_{inlet}} = 10,095 \tag{4.2}$$

They are two of the most important quantities for the characterization of this impinging jet configuration.

4.2 Numerical Setup

4.2.1 Mesh

The above mentioned impinging jet configuration is simulated in two separate studies, which primarily differ in their numerical grids. These two studies are referred to as study A and study B. Study A is carried out with an unstructured grid including the plenum. Study B, on the other hand, is based on a block-structured grid. Its setup does not include a plenum in order to reduce computational costs. The numerical grids of both studies are illustrated in Figure 4.4. More detailed views of the grid of study B are given in Appendix B.1. This work is focussed on study B and its results, which is why study A will not be discussed in detail, but only used for reference purposes within the RANS study.

In order to simplify the variation of the grid resolution, a grid factor is introduced for the block-structured grid of study B. The number of grid lines in each spatial direction is proportional to this factor. As a consequence, doubling the grid factor increases the number of grid cells by eight times. The numbers of grid cells for study A and for each of the relevant grid factors of study B are given in Table 4.5. The difference between the RANS and LES grid with grid factor 4 is due to minor grid modifications that were made between the two studies. Further details about the cell numbers of the duct and the nozzles are given in Appendix B.1.

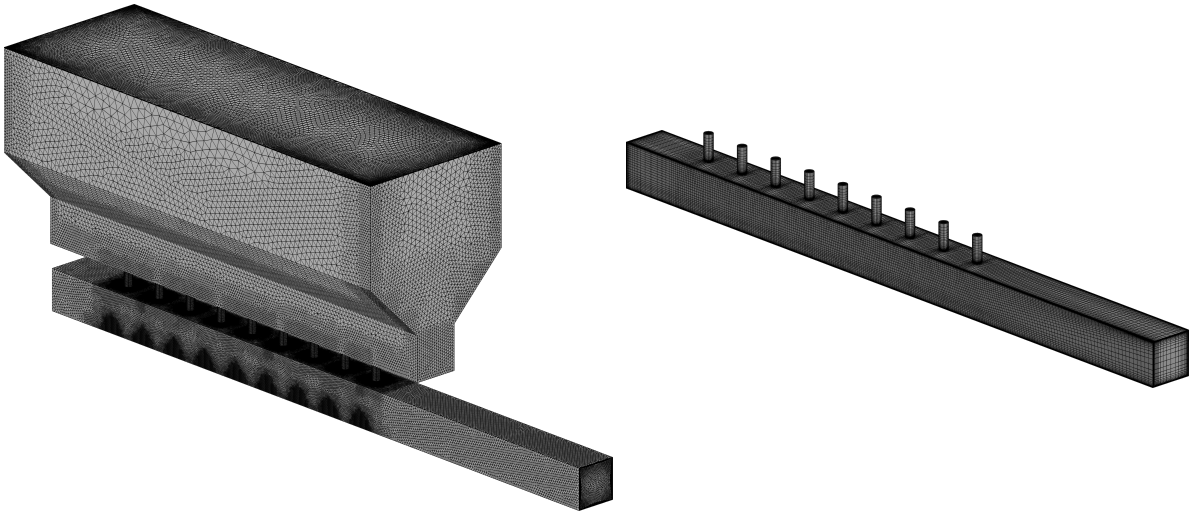

Study A
(unstructured)

Study B
(block-structured, grid factor 1)

Figure 4.4: Three dimensional view of the numerical grids of study A and study B

Table 4.5: Number of grid cells for study A and for relevant grid factors of study B

Grid	Number of grid cells
Study A	19,702,431
Study B, grid factor 1	RANS: 552,348
Study B, grid factor 2	RANS: 4,418,784
Study B, grid factor 3	RANS: 14,913,396
Study B, grid factor 4	RANS: 35,350,272, LES: 34,230,528
Study B, grid factor 5	LES: 66,856,500

The grid is designed in such a way that it fulfils the condition of a low Reynolds number grid for almost the entire domain: The node that is next to the wall has to be located at a non-dimensional distance wall coordinate of $y^+ \leq 1$. y^+ is defined by following equation and is based on the shear velocity u_τ.[4]

$$y^+ = \frac{\rho u_\tau y}{\mu} \qquad u_\tau = \sqrt{\frac{\tau_{wall}}{\rho}} \tag{4.3}$$

The coordinates of the nodes that are next to the wall are invariant to changes of the grid factor. Contour plots of the non-dimensional distance wall coordinates of these nodes are given in Appendix B.1 for a RANS simulation with grid factor 4.

4.2.2 Boundary Conditions

Boundary conditions are applied to every surface of the computational domain. These surfaces are categorized as inlets, outlet, heating plate and walls (see Figure 4.6). Two distinct inlet boundary conditions are defined for study B: The uniform inflow and the inflow profiles boundary condition. The aim of these inlet boundary conditions is to reproduce the characteristics of the flow coming from the plenum.

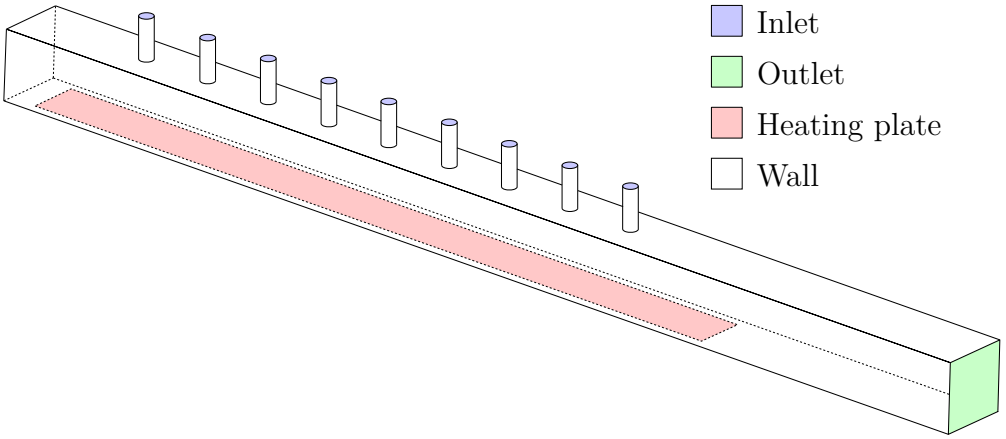

Figure 4.6: Visualization of different surface categories (drawing not in scale)

For the *uniform inflow* boundary condition, a profile is used whose flow parameters are constant over the entire inflow area. It is based on the assumption that there is no boundary layer at the inlet of the nozzle. The respective flow parameters are given in Table 4.7.

The *inflow profiles* boundary condition, on the other hand, is defined by a two-dimensional distribution of flow parameters, which is obtained from the results of study A. These profiles include the turbulent kinetic energy, the specific dissipation rate, the total pressure, the total temperature and a velocity direction vector. They are interpolated on the respective surface grid of the inlet. The total pressure is plottet in Figure 4.8 as an example of these inflow profiles.

For the RANS studies, a constant mass flow of 0.01998 kg/s is defined as an outlet boundary condition. The static pressure at the outlet is permanently adjusted to keep the mass flow at this level. For the LES study, on the other hand, a constant static pressure of 101,947 Pa is defined for the outlet, since the automatic readjustment of the mass flow would take too long to reach a steady state due to the low flow velocities. The wall and the heating plate are modelled as no-slip walls. A heat flux of 5000 W/m^2 is applied to the heating plate, while the remaining walls are adiabatic.

Table 4.7: Flow parameters of the uniform inflow boundary condition

Variable	Value
Total pressure p_{inlet}	102,042 Pa
Flow direction	$\begin{pmatrix} 0 & 0 & -1 \end{pmatrix}^\top$
Total temperature T_{inlet}	298.2 K
Turbulence intensity	0.01
Eddy length scale	0.003 m

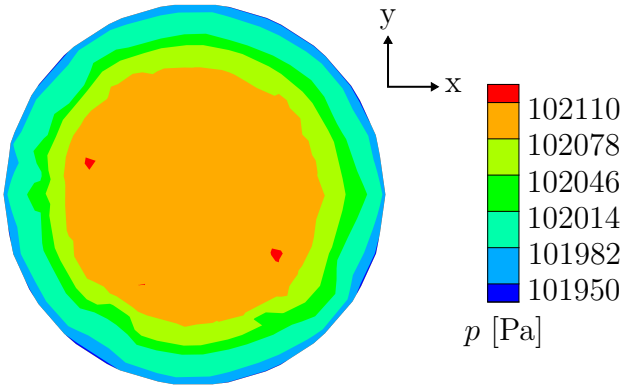

Figure 4.8: Example of an inflow profile: Contour plot of the total pressure (nozzle 5)

4.2.3 Gas Model

Two gas models are used to compute the major physical properties of the considered fluid: The ideal gas model and the Sutherland model. Additionally, the Prandtl number is assumed to be constant.

The *ideal gas model* provides a relation between p, ρ and T with the gas constant R [38].

$$p = \rho R T \tag{4.4}$$

The specific internal energy e and the specific enthalpy h can be related to the temperature T via c_v and c_p [4].

$$e = c_v T \qquad h = c_p T \tag{4.5}$$

The specific heat capacities are obtained from following equations [4].

$$c_p = \frac{R}{1 - \frac{1}{\kappa}} \tag{4.6}$$

$$c_v = c_p - R \tag{4.7}$$

The *Sutherland model* is used to evaluate the viscosity of a gas, which is described as a function of T, the Sutherland's law constant C_{su}, the reference temperature T_0 and the reference viscosity μ_0 [1].

$$\mu = \mu_0 \frac{T_0 + C_{su}}{T + C_{su}} \left(\frac{T}{T_0}\right)^{\frac{3}{2}} \tag{4.8}$$

The thermal conductivity is obtained from Pr (see Section 2.2.1) and μ. Table 4.9 lists the gas model parameters that are used for this study.

Table 4.9: Setting of parameters for the ideal gas model, the Sutherland model and Pr

Variable	Value
R	287.06 J/(kg·K)
κ	1.4
C_{su}	110 K
T_0	273 K
μ_0	$1.7198 \cdot 10^{-5}$ Pa·s
Pr	0.72

5 RANS Simulation

The focus of this chapter lies on the RANS simulations that are carried out prior to the LES study. The numerical background of the RANS study is briefly discussed with additional information given on time discretization. The convergence behaviour of the various RANS setups is evaluated thereafter. Then, the results of the grid study are presented with a particular focus on the heat transfer characteristics. This also includes an evaluation of grid independence. An additional sensitivity study gives an insight on how the system reacts to changes in heat flux and mass flow. Finally, a scaling approach to reduce computational costs for the later LES is discussed.

5.1 Numerical Background

The RANS study is conducted using the CFD solver TRACE, which is being developed by the DLR. It solves the Favre-averaged compressible Navier-Stokes equations with the finite volume method. Several steady RANS simulations are carried out with grid factors 1 to 4 and the uniform inflow as well as the inflow profiles boundary condition. The turbulence model selected for this study is the SST k-ω model (see Section 3.2.3).

The simulations are carried out with 100,000 pseudo time steps in order to reach a steady state (see Section 5.2). Each pseudo time step is defined by the *Courant-Friedrichs-Lewy number* CFL, which is a non-dimensional parameter for the numerical setup. In the one-dimensional case, it gives an estimate of how far the fluid with the velocity u moves through a cell with the spatial dimension Δx during one pseudo time step $\Delta\tau$.[4, 14] Since acoustic effects are involved, the speed of sound a is included in the equation.

$$CFL = \frac{(u+a)\Delta\tau}{\Delta x} \tag{5.1}$$

The procedure used by TRACE to calculate the CFL number in the three-dimensional case is not further discussed in this work. The solver settings for the RANS simulations are given in Appendix C.1.

5.2 Convergence

The residual is an indicator for the convergence of an iterative numerical solution. Each cell in the domain has its own residual. It describes the error of an approximation to the respective mathematical solution of an equation and is used to determine whether a computation reaches a steady state. Theoretically, this is considered to be the case when the residual equals 0. However, this is practically impossible for numerical simulations, so that low residuals and oscillations have to be accepted as a criterion for convergence.[1, 14]

Normalized (or global) residuals are used to study the convergence behaviour of the entire domain. There are different normalization procedures available within TRACE, one of which gives the L1 residuals (the procedure is described in Appendix C.2). They are given in Figure 5.1 for grid factors 1 to 4 with the uniform inflow and the inflow profiles boundary condition. It should be noted that the setups are not marked separately, as there are no significant differences between their residuals.

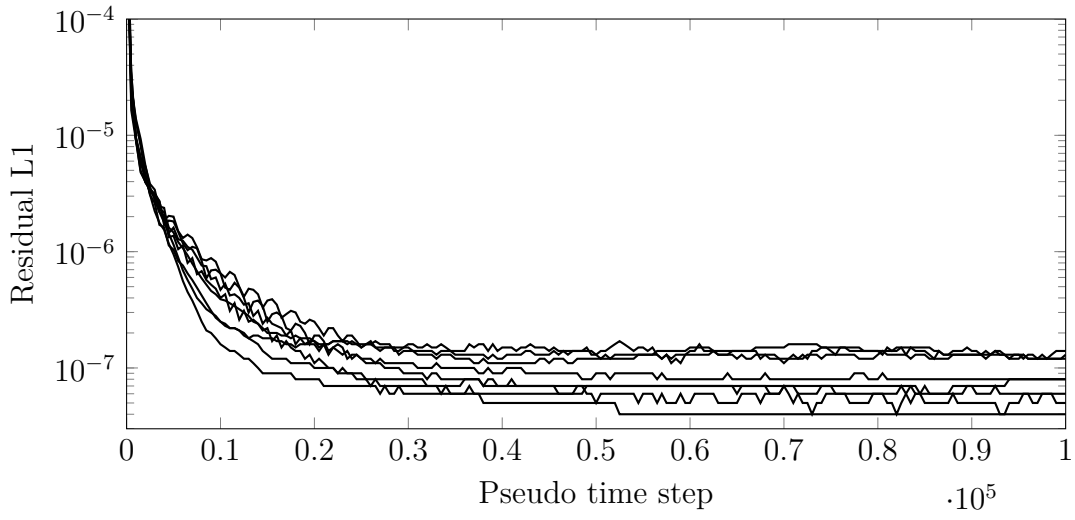

Figure 5.1: L1 residuals for grid factors 1 to 4 with uniform inflow and inflow profiles

According to these residuals and taking into account that steady RANS simulations are carried out for a rather unsteady flow situation, it can be considered that the simulation of each setup reaches a steady state. The number of pseudo time steps is sufficient, so that the residuals converge to a low value without large oscillations.

5.3 Grid Study

The focus of this study lies on the heat transfer characteristics of the considered impinging jet configuration, for which the Nusselt number is regarded as the most important indicator. Therefore, Nusselt numbers are computed for the entire target plate including the heating plate. They are obtained by using following equation [27].

$$Nu = \frac{q_{hp} D}{\lambda (T - T_{inlet})} \tag{5.2}$$

As proposed by Brakmann [6], the Nusselt numbers considered in this work are scaled with $Re_{inlet}^{2/3}$ in order to allow better comparability with other test cases. Unless otherwise stated, Re_{inlet} of 10,095 will be used for this purpose. An overview of the velocity field in the domain and the temperature distribution on the target plate is given in Figure 5.2 in the form of contour plots.

In the following subsection, the area averaged Nusselt numbers are presented for different setups. For a better understanding of the local distribution of heat transfer, the spanwise averaged Nusselt number distributions are discussed thereafter. Based on the spanwise averaged Nusselt numbers, the grid convergence is then evaluated.

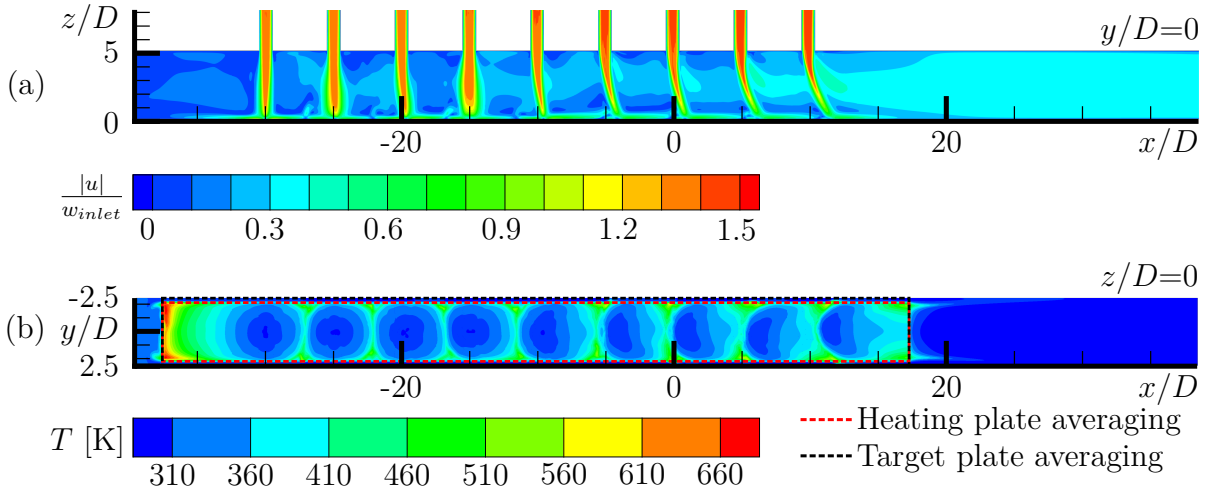

Figure 5.2: Contour plots of the velocity magnitude $|u|$ scaled with $w_{inlet} = 10.263$ m/s at $y/D = 0$ (a) and the temperature T on the target plate for grid factor 4 and the inflow profiles boundary condition (b)

5.3.1 Area Averaged Nusselt Numbers

The purpose of the area averaged Nusselt numbers is to provide an overview of the heat transfer characteristics of different impinging jet configurations. They are later compared to correlations from the literature in Section 6.4.1. In this study, the area averages are considered separately for the entire target plate and the heating plate (see Figure 5.3). Target plate averaging is defined as averaging over the entire heating plate area plus the two gaps between the heating plate and the side walls (see Figure 5.2).

For the considered impinging jet configuration, RANS simulations with particularly coarse grids, such as with grid factor 1, result in comparatively low Nusselt numbers. The coarse level of resolution causes inaccuracies in the prediction of velocity gradients and therefore the heat transfer. Between grid factors 2 and 4, however, a convergent behaviour becomes apparent (see Section 5.3.3). Furthermore, Nusselt numbers are higher with the inflow profiles than with the uniform inflow boundary condition, since the boundary layers and therefore the turbulence in the nozzles are more pronounced with inflow profiles. The target plate averaged Nusselt numbers are slightly higher than the heating plate averaged Nusselt numbers. This is due to the relatively low temperature levels at the two gaps between heating plate and side walls as well as the way the Nusselt number is computed. Since the Nusselt number is computed with the same heat flux of 5,000 W/m^2 at every position on the target plate, a decrease in temperature increases the Nusselt number.

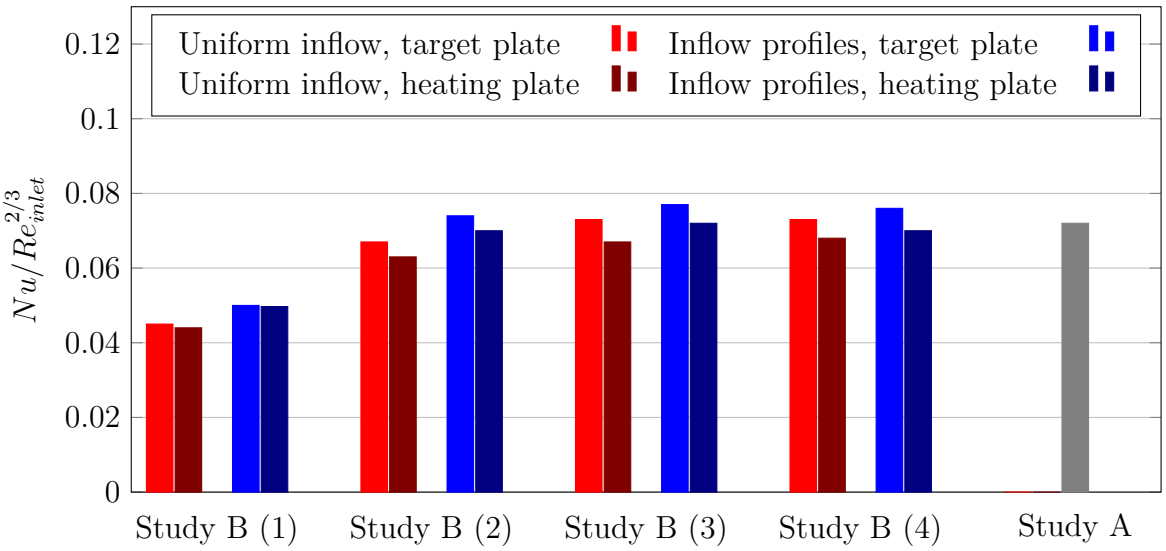

Figure 5.3: Target plate and heating plate averaged Nusselt numbers for study B (grid factors 1 to 4) as well as for study A (heating plate averaged)

5.3.2 Spanwise Averaged Nusselt Number Distributions

Nusselt number distributions provide data about the local heat transfer on the target and heating plate. In this study, these distributions are generated by spanwise averaging (in y-direction) the Nusselt numbers on the heating plate. They are given in Figure 5.4 for the uniform inflow and in Figure 5.5 for the inflow profiles boundary condition. Additionally, the results of study A are provided as a reference.

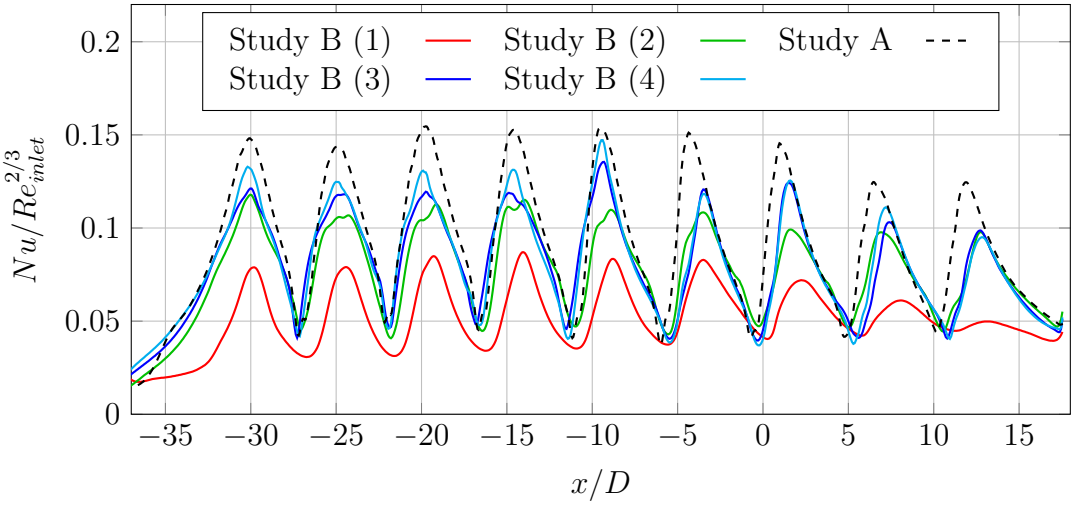

Figure 5.4: Uniform inflow: Heating plate spanwise averaged Nusselt number distribution for grid factors 1 to 4 together with the reference solution from study A

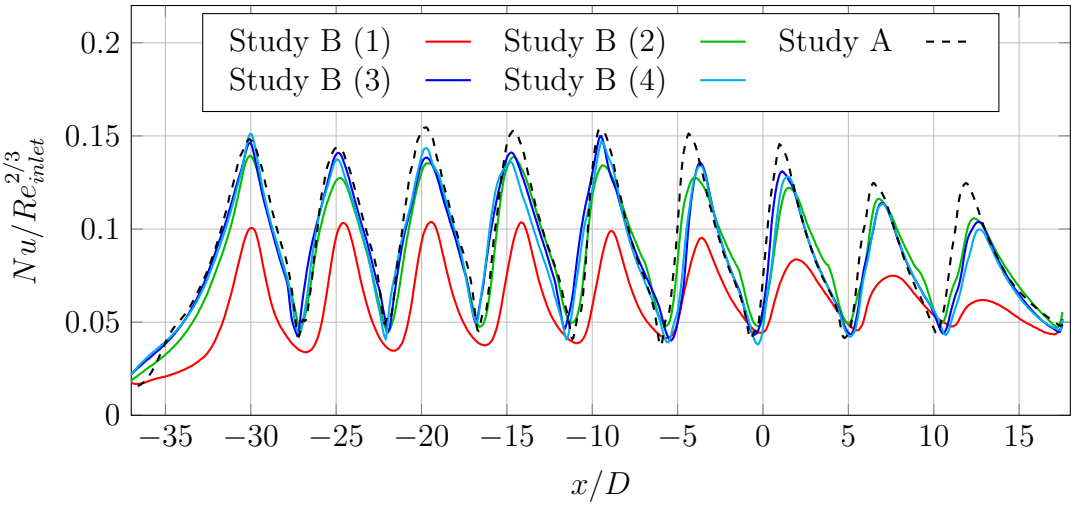

Figure 5.5: Inflow profiles: Heating plate spanwise averaged Nusselt number distribution for grid factors 1 to 4 together with the reference solution from study A

The plots show nine peaks occurring at the stagnation point of each impinging jet,

which is an indicator for high heat transfer rates in these regions. However, the Nusselt number decreases in downstream direction as the effect of cross-flow increases near to the outlet. That is in good agreement with the results of References [25, 40, 43]. The amplitudes of the Nusselt number distributions for the various grid factors and boundary conditions differ significantly from each other. For example, heat transfer rates are clearly underestimated for coarse grids, which is already shown for the area averaged results from Section 5.3.1.

The Nusselt number distributions for the inflow profiles show higher grid convergence compared to those for the uniform inflow boundary condition (see Section 5.3.3). Additionally, they get closer to the reference distribution from study A, which is due to the fact that the inflow profiles are derived from this study.

5.3.3 Grid Convergence Index

The *grid convergence index* (GCI) method [7] is used to draw conclusions about the convergence behaviour over several numerical grids. It aims at the comparability to grids from other literature sources. The method is applied to the results of simulations with the uniform inflow and the inflow profiles boundary condition. It requires three systematically refined grids, for which grid factors 2, 3 and 4 are selected. The procedure is described in Appendix C.3.

The heating plate averaged approximated relative error e_a^{21}, extrapolated relative error e_{ext}^{21} and fine-grid convergence index GCI_{fine}^{21} are given in Table 5.6. Each of these three variables indicates higher grid convergence for the setup with the inflow profiles compared to the setup with the uniform inflow boundary condition.

Table 5.6: Heating plate averaged e_a^{21}, e_{ext}^{21} and GCI_{fine}^{21} for the uniform inflow and the inflow profiles boundary condition

	Uniform inflow	Inflow profiles
Heating plate averaged e_a^{21}	5.194 %	4.850 %
Heating plate averaged e_{ext}^{21}	2.559 %	1.806 %
Heating plate averaged GCI_{fine}^{21}	3.198 %	2.258 %

Additionally, it is recommended in Reference [7] to provide further data about the local error distributions. Figures 5.7 and 5.8 show the spanwise averaged Nusselt number distributions for grid factor 4 with error bars. The error bars indicate the extrapolated

absolute error $e^{21}_{ext,abs}$, which is described in Appendix C.3. For both cases, large errors particularly occur at the stagnation points and in regions of low Nusselt numbers between the jets. However, this effect is more pronounced for the results of the uniform inflow computations. The production of large errors at stagnation points is a general disadvantage of two-equation models [2]. Nevertheless, the mesh is regarded as being sufficiently accurate for the scope of this study.

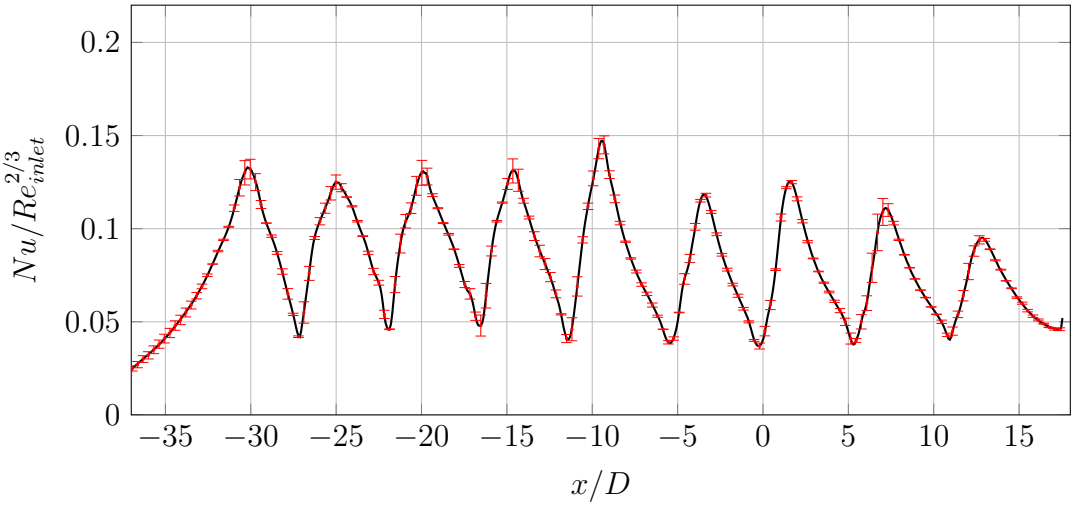

Figure 5.7: Uniform inflow: Heating plate spanwise averaged Nusselt number distribution with error bars for grid factor 4

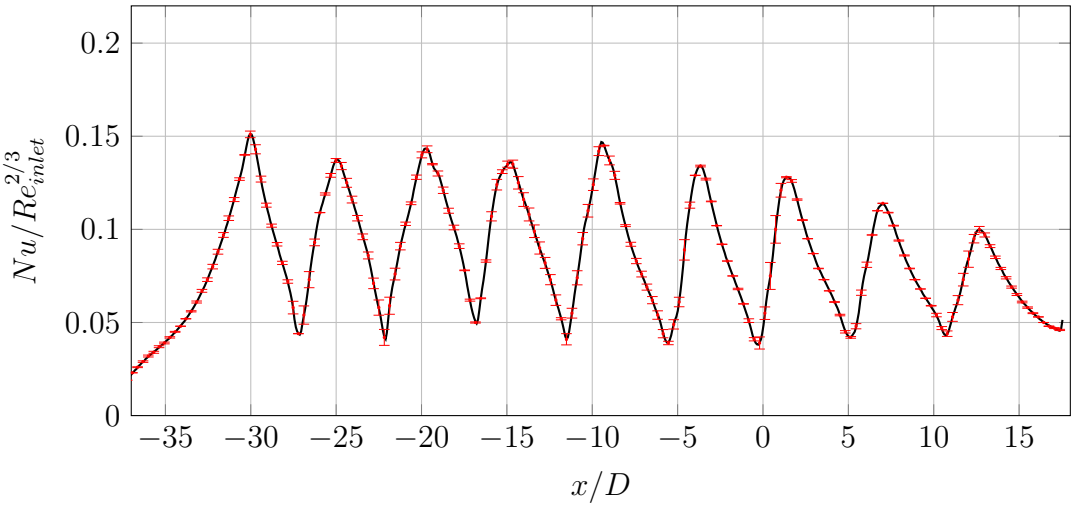

Figure 5.8: Inflow profiles: Heating plate spanwise averaged Nusselt number distribution with error bars for grid factor 4

5.4 Sensitivity Study

Since a comparison with experimental data is planned for subsequent studies, a sensitivity study is carried out. It is assumed that boundary conditions such as mass flow and heat flux can not be adjusted with the same accuracy in the experiments as in the numerical simulations. Therefore, the effects of possible deviations on the heat transfer should be estimated with further RANS simulations.

As part of the sensitivity study, four RANS simulations are carried out with grid factor 3 and inflow profiles. Within each simulation, either the mass flow or the heat flux is changed by +50 % and –50 %, while all other parameters remain unchanged. The results are compared to a reference solution from a simulation with unchanged parameters in Figure 5.9.

The Nusselt number distributions are strongly influenced by changes in mass flow. An increase in mass flow causes an increase in heat transfer and thus the Nusselt number. However, this effect is compensated in Figure 5.9 by scaling the Nusselt numbers with $Re^{2/3}$ ($\dot{m}_{target} \times 1.5$: $Re_{inlet} = 15,143$, $\dot{m}_{target} \times 0.5$: $Re_{inlet} = 5,048$).

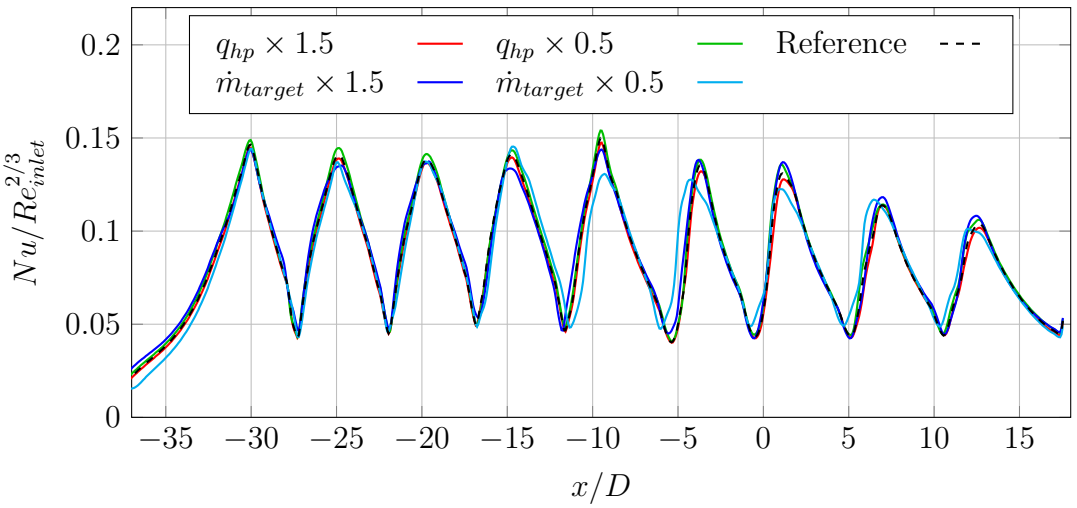

Figure 5.9: Inflow profiles: Heating plate spanwise averaged Nusselt number distributions for grid factor 3 with increased and decreased heat flux and mass flow compared to an unchanged reference solution

5.5 Scaling Approach

In order to reduce the computational costs for the later LES, two approaches to scale the numerical domain are tested as part of the RANS study. The idea behind the scaling is to reduce the number of required time steps per number of through flows through the domain. Therefore, the domain is scaled down by a factor of 10 in each spatial direction. Certain flow variables have to be adjusted accordingly in order to keep the relevant non-dimensional parameters at a constant level. It should be noted that scaling can only be regarded as beneficial if it does not change the value of CFL, because otherwise the condition of $CFL \leq 1$ may be violated.

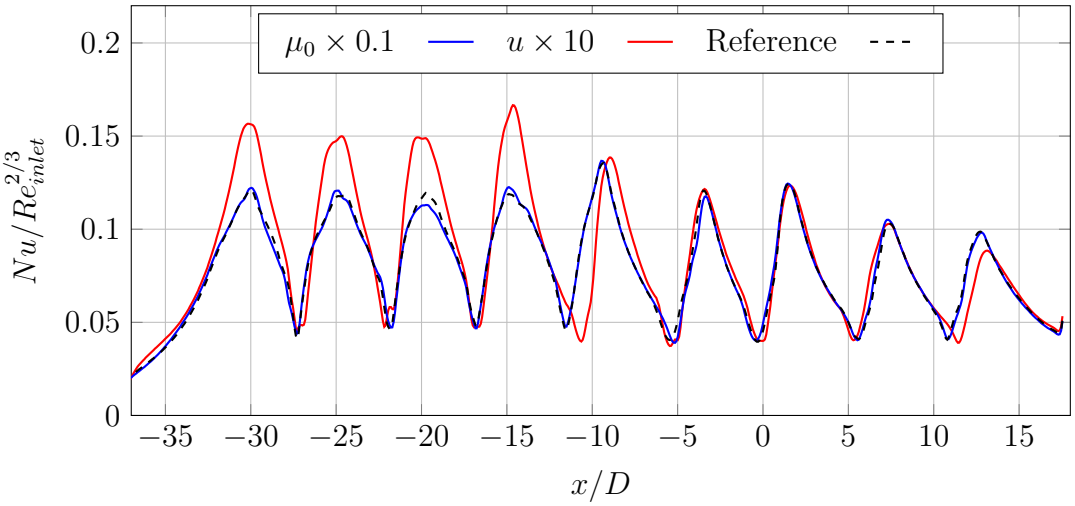

Figure 5.10: Uniform inflow: Heating plate spanwise averaged Nusselt number distributions for grid factor 3 with the scaled setups and the unscaled reference setup

The first approach ($\mu_0 \times 0.1$) serves as a proof that scaling delivers Nusselt number distributions that correspond to the unscaled results. Therefore, the domain is scaled while keeping Re, Ma and Pr at a constant level. Consequently, the reference viscosity μ_0 has to be reduced by a factor of 10. Additionally, the mass flow is reduced by a factor of 100 in order to reduce the velocity by a factor of 10. The downscaling in each spatial direction increases the through flow frequency by 10 times, because the velocity remains constant. Since the time step must also be decreased by 10 times in order to meet the CFL condition, the number of required time steps for one through flow does not change and therefore there is no benefit. However, the first approach shows that scaling is generally possible with this setup, so that the Nusselt number distribution of the scaled setup corresponds to the unscaled result (see Figure 5.10).

With the second approach ($u \times 10$), Re is kept constant by increasing the velocity u

by 10 times. The increase in speed and the decrease in length scale result in an increase in through flow frequency by 100 times. In order to meet the CFL condition, the time step is decreased by a factor of ≈10. Consequently, the number of required time steps is reduced by ≈10 times compared to an unscaled setup, which theoretically would be a significant benefit. However, the Nusselt number distribution does not correspond to the unscaled reference result (see Figure 5.10). It is suspected that changes in Mach number and changed heat transport and cross-flow conditions cause these differences.

As a consequence, the scaling approach is not used for the LES study. Nevertheless, the results of the scaling approaches are still considered worth mentioning, as they might be useful for further investigations. The factors, by which the parameter settings are changed in relation to the unscaled reference setup, are given in Table 5.11.

Table 5.11: Factor, by which parameter settings are changed in relation to the unscaled reference setup for the first and second approach ($\mu_0 \times 0.1$ and $u \times 10$)

	$\mu_0 \times 0.1$	$u \times 10$
Δx	×0.1	×0.1
Δt	×0.1	×0.08
u	×1	×10
μ_0	×0.1	×1
Mass flow	×0.01	×0.1
Through flow frequency	×10	×100
Required number of pseudo time steps	×1	×0.13

6 Large Eddy Simulation

This chapter focusses on the implementation and evaluation of the LES study. In the first part, crucial information relating to the solver settings and probe positions is provided. The simulation quality is then evaluated especially regarding grid resolution, statistical convergence and energy spectra. Finally, the velocity field and heat transfer characteristics are compared to the results obtained from the RANS studies and correlations from the literature.

6.1 Numerical Background

Within this LES study, TRACE solves the Favre-filtered compressible Navier-Stokes equations by applying the finite volume method and *MUSCL* (Monotonic Upstream-centered Scheme for Conservation Laws) reconstruction with $\kappa = 1/3$ [17]. Two LES are conducted using the slightly modified block-structured grids from RANS study B with grid factors 4 and 5 (see Table 4.5) with the inflow profiles boundary condition. It is assumed that their resolutions meet the demands of an LES. The SGS model used for this study is the WALE model with $C_w = 0.5587$ (see Section 3.3.2).

The LES is carried out using an explicit time scheme. A converged RANS simulation is used for the initialization of the LES. The results are analysed after 1,900,000 time steps or ≈30 through flows through the nozzle (based on the averaged z-velocity $\bar{w}_{nozzle7}$ within nozzle 7 and the nozzle length l_{nozzle}). In order to meet the condition of $CFL \leq 1$ for the smallest cell in the domain, a constant time step of $7.5{\cdot}10^{-8}$ s is chosen. The smallest cell is next to the wall and therefore invariant to changes of the grid factor, as mentioned earlier in Section 4.2.1. The solver settings for the LES are given in Appendix D.1.

With TRACE, LES typically are conducted with a fraction of 0.1 % of *Roe's numerical flux* [34] added to the central flux [17]. This fraction is referred to as the *blending factor*. In this case, undesired peaks in the high wave number range of the energy spectrum were observed for a blending factor of 0.1 %. This issue was solved by setting the blending

factor to 1 %.

The time series of certain flow variables are of great interest for this LES study (see Section 6.2.3). However, recording this data for each cell of the domain would be too memory consuming. Therefore, virtual probes are installed at preselected positions in the domain to gather those time series. The probes are located at the target plate, a center slice at $y/D = 0$ and the center of nozzles 1-9. Additionally, a large number of probes is positioned within and below nozzle 7. An overview of the probe positions is given in Figure 6.1.

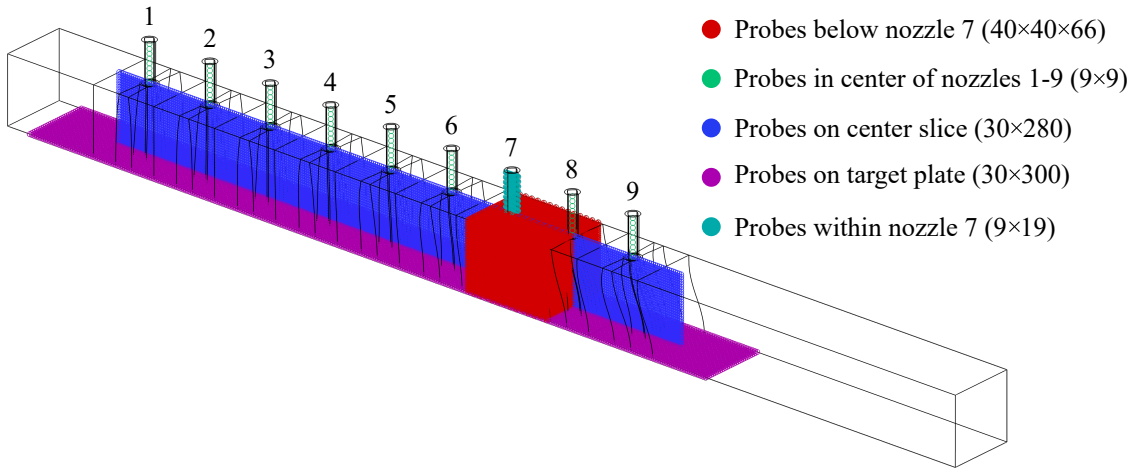

Figure 6.1: Visualization of the probe positions with the number of probes given for each category as well as a schematic visualization of the domain boundaries

6.2 Simulation Quality

Before evaluating the results of the simulations, four important quality features are considered. They are related to the operation point, the grid resolution, the statistical convergence of flow quantities and the power spectral densities.

6.2.1 Operation Point

As already mentioned in Section 4.2.2, the static pressure at the outlet is set to 101,947 Pa to achieve the desired target mass flow of 0.01998 kg/s. Therefore, the deviation from the time signal of the outlet mass flow $\dot{m}$ to the target mass flow $\dot{m}_{target}$ has to be determined.

The deviation is plotted over the number of time steps in Figure 6.2 for grid factors

4 and 5. For both grid factors, the time signal of $\dot{m}$ converges to a value slightly below $\dot{m}_{target}$. Since the predicted pressure losses in the domain are different between the two simulations, $\dot{m}$ is closer to $\dot{m}_{target}$ with grid factor 5 than with grid factor 4. However, the deviations of both simulations are within an acceptable range.

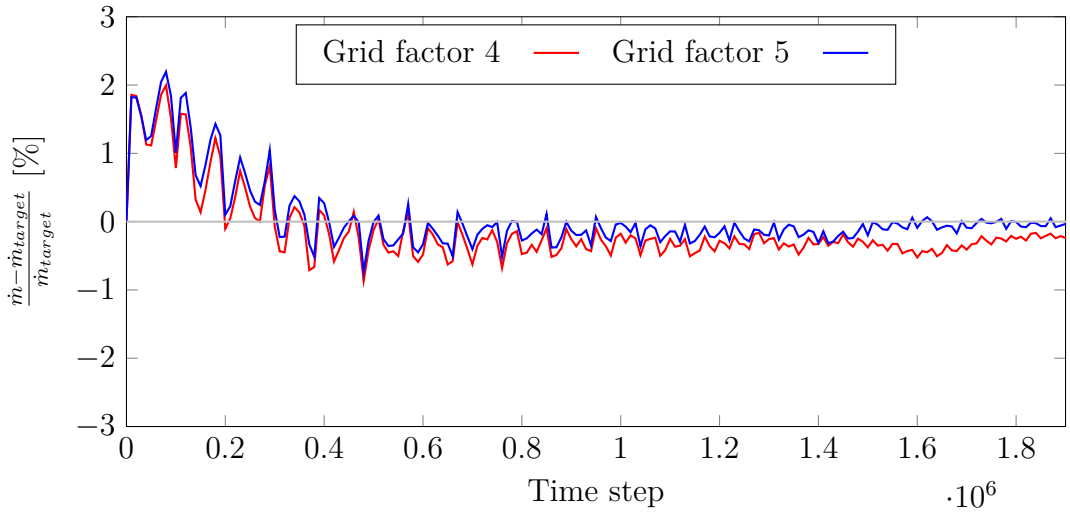

Figure 6.2: Deviation from the time signal of the mass flow $\dot{m}$ to the target mass flow $\dot{m}_{target}$ for grid factors 4 and 5

6.2.2 Grid Resolution Suitability

To provide further information about the grid resolution suitability, the spatial cut-off scales $\Delta_{cut} = V^{\frac{1}{3}}$ are assessed in relation to the Favre-averaged Kolmogorov length scales $\tilde{l}_\eta$. Figure 6.3 shows contour plots of $\frac{\Delta_{cut}}{\tilde{l}_\eta}$ for grid factors 4 (Figure 6.3a) and 5 (Figure 6.3b).

The Kolmogorov length scales are computed as stated in Section 2.2.2 using the dissipation rate ε. ε represents the trace of the dissipation rate tensor ε_{ij}, which in this case is approximated using the resolved velocity gradients, the dynamic viscosity μ and the trace-free strain rate tensor S^*_{ij}.

$$\varepsilon = \frac{1}{2}\varepsilon_{ii} \qquad \varepsilon_{ij} \approx \frac{2}{\bar{\rho}}\overline{\left(\mu S^*_{kj}\frac{\partial u''_i}{\partial x_k} + \mu S^*_{ki}\frac{\partial u''_j}{\partial x_k}\right)} \qquad S^*_{ij} = S_{ij} - \frac{1}{3}S_{qq} \tag{6.1}$$

According to Fröhlich et al. [16], a substantial part of the dissipation is resolved with $\frac{\Delta_{cut}}{\tilde{l}_\eta} \leq 12$. Figure 6.3 indicates that the grids with grid factors 4 and 5 both fulfil this condition. There are only a few scattered regions in the domain where the ratio is slightly

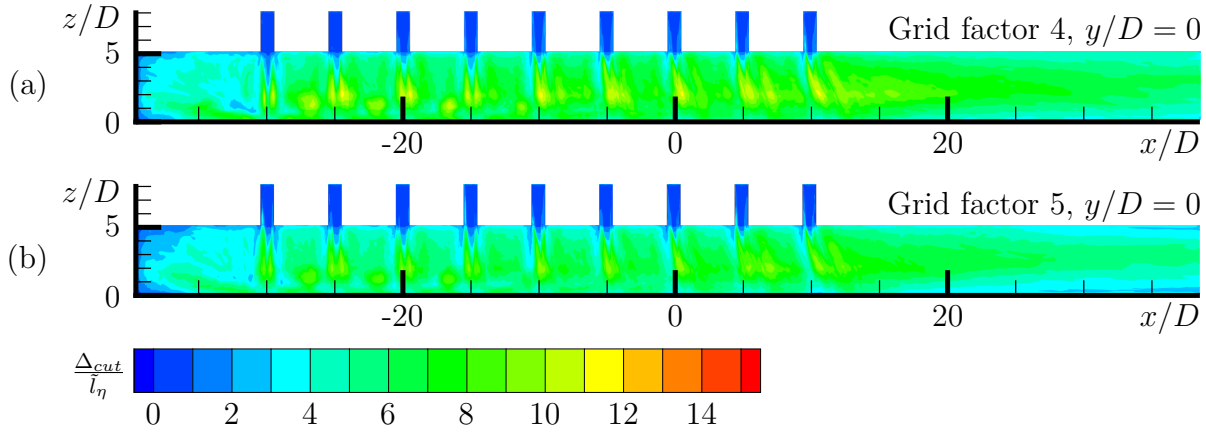

Figure 6.3: Contour plots of $\frac{\Delta_{cut}}{l_\eta}$ at $y/D = 0$ for grid factors 4 (a) and 5 (b)

above the limit and which are not covered by this plot. Therefore, the grid resolutions are considered to meet the demands of this LES study. It should be noted that Fröhlich et al. take another and more conservative approach to compute ε: They determine the imbalance in the terms of the transport equation of the Reynolds stresses. This approach leads to higher values of $\frac{\Delta_{cut}}{l_\eta}$ compared to the approach that is used for this test case.

6.2.3 Statistical Convergence

To assess the statistical convergence of the LES, the mean and error values of preselected time-dependent flow variables within and below nozzle 7 are examined. The undesired fluctuations from the initial phase of the simulation, i.e., the initial transient, have to be removed from a time signal before computing its mean and error values. Therefore, the index of the final sample d^* of the initial transient must be determined by solving the following minimization problem with the sample index d, the total number of samples N, the flow variable ϕ and its truncated mean value $\bar{\phi}_{N,d}$.[3]

$$d^* = \underset{0<d\leq N}{\arg\min} \underbrace{\left[\frac{1}{(N-d)^2}\sum_{i=d}^{N-1}\left(\phi_i - \bar{\phi}_{N,d}\right)^2\right]}_{\text{running variance}} \tag{6.2}$$

$$\bar{\phi}_{N,d} = \frac{1}{N-d}\sum_{i=d}^{N-1}\phi_i \tag{6.3}$$

Figure 6.4 illustrates the above mentioned procedure by showing an example of a velocity time signal w, its mean value $\bar{w}$, its running variance and the end of its initial transient. It should be noted that the fluctuations are relatively small for this example,

as it is taken from the center of nozzle 7. They are considerably larger in the boundary layer and in the free jet region below.

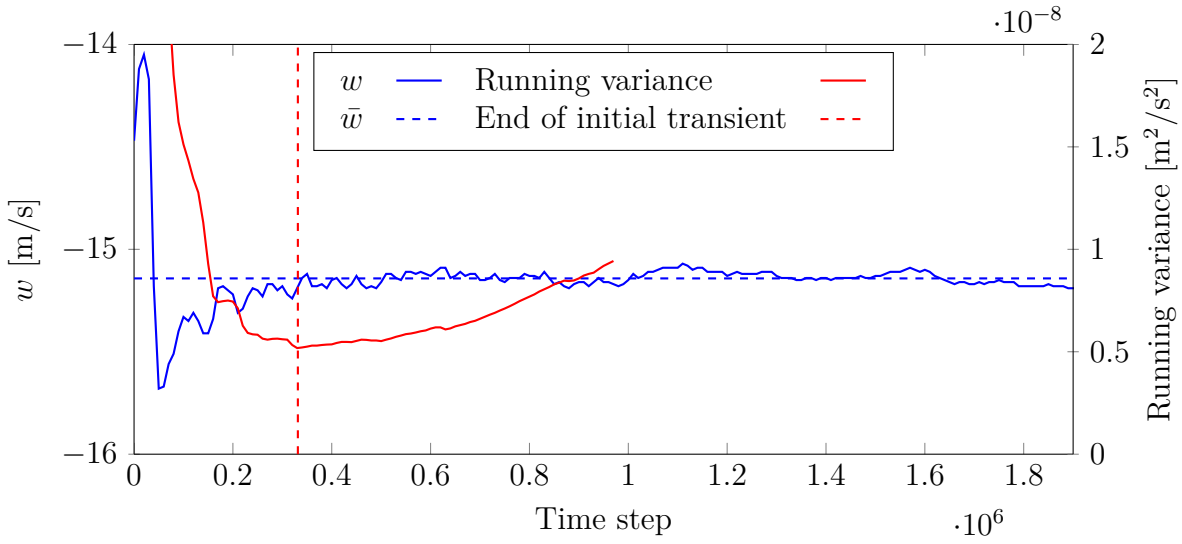

Figure 6.4: An example of a velocity time signal w within nozzle 7, its mean value $\bar{w}$, its running variance and the end of its initial transient (probe position $x/D = 0$, $y/D = 0$, $z/D = 6.01$)

Since the initial transients of all considered time signals end at similar positions, the averaging start is set to 500,000 time steps. Taking the averaged velocities within and below nozzle 7 into account, the fluid flows ≈22 times through the nozzle and ≈5 times from the nozzle to the target plate during the averaging interval.

For the following procedure it is assumed that the initial transient has successfully been removed from the time signal. The estimated error $e_N(\bar{\phi})$ is defined as the difference between the expected population value $E(\phi)$ and the sample mean $\bar{\phi}$.

$$e_N(\bar{\phi}) = \bar{\phi} - E(\phi) \tag{6.4}$$

$$\bar{\phi} = \frac{1}{N} \sum_{i=0}^{N-1} \phi_i \tag{6.5}$$

Since $E(\phi)$ is generally unknown due to the finite simulation time, $e_N(\bar{\phi})$ has to be computed using the following approximation with the minimal number of samples between two independent observations N_d and the population variance $\mathrm{Var}_N(\phi)$.

$$e_N^2(\bar{\phi}) \approx \frac{N_d \mathrm{Var}_N(\phi)}{N} \tag{6.6}$$

$$\mathrm{Var}_N(\phi) = \frac{1}{N}\sum_{i=0}^{N-1}(\phi_i - \bar{\phi})^2 \tag{6.7}$$

N_d is defined by following equation, where ρ_τ represents the unknown autocorrelation of the samples with the lag τ.

$$N_d = 1 + 2\sum_{\tau=1}^{N}\left(1 - \frac{\tau}{N}\right)\rho_\tau \tag{6.8}$$

$$\rho_\tau = \frac{\frac{1}{N-\tau}\sum_{i=\tau}^{N-1}\left(\phi_i - \bar{\phi}\right)\left(\phi_{i-\tau} - \bar{\phi}\right)}{\mathrm{Var}_N(\phi)} \tag{6.9}$$

$e_N(\bar{\phi})$ can be used to define a confidence interval CI for the statistical quantity ϕ. Assuming a normal distribution, the 68 % and 95 % CI can be determined as follows.[3]

$$CI_{68\%} \approx \left[\bar{\phi} - 1e_N(\bar{\phi}); \bar{\phi} + 1e_N(\bar{\phi})\right] \tag{6.10}$$

$$CI_{95\%} \approx \left[\bar{\phi} - 1.96e_N(\bar{\phi}); \bar{\phi} + 1.96e_N(\bar{\phi})\right] \tag{6.11}$$

Figures 6.5 and 6.6 show the mean values $\bar{w}$ and estimated errors $e_N(\bar{w})$ for the z-component w of the velocity vector. Figures 6.7 and 6.8 show the mean values $\bar{k}$ and estimated erros $e_N(\bar{k})$ for the resolved turbulent kinetic energy k.

$$k = \frac{1}{2}u_i' u_i' \tag{6.12}$$

The contour plots are taken from a center slice at $y/D = 0$ within and below nozzle 7 for grid factors 4 and 5.

The estimated errors $e_N(\bar{w})$ and $e_N(\bar{k})$ are significantly larger in the free jet region below compared to the pipe flow within the nozzle. This also applies to the magnitude of k. Additionally, $e_N(\bar{k})$ is larger compared to $e_N(\bar{w})$, since k is a second-order moment quantity. Those quantities generally take longer to converge, i.e., a larger amount of time steps is necessary to reduce $e_N(\bar{k})$ [3, 15]. However, the estimated errors are smaller with grid factor 5 than with grid factor 4, indicating that the simulation with grid factor 5 is better converged. The velocity fields, on the other hand, are similar for both meshes.

In total, the estimated errors $e_N(\bar{w})$ and especially $e_N(\bar{k})$ are relatively large. A higher amount of through flows, i.e., time steps, are necessary to reduce those errors to an acceptable level. However, the expense of higher computational costs was not within the time limit of this study. For technical reasons, the time signals for the Nusselt numbers

on the heating plate were not recorded. Consequently, detailed statistical data is not available for them. Nevertheless, they are presumed to be converged with smaller errors than w and k. The simulation is therefore considered to meet the demands of this study, whose main focus lies on the heat transfer characteristics.

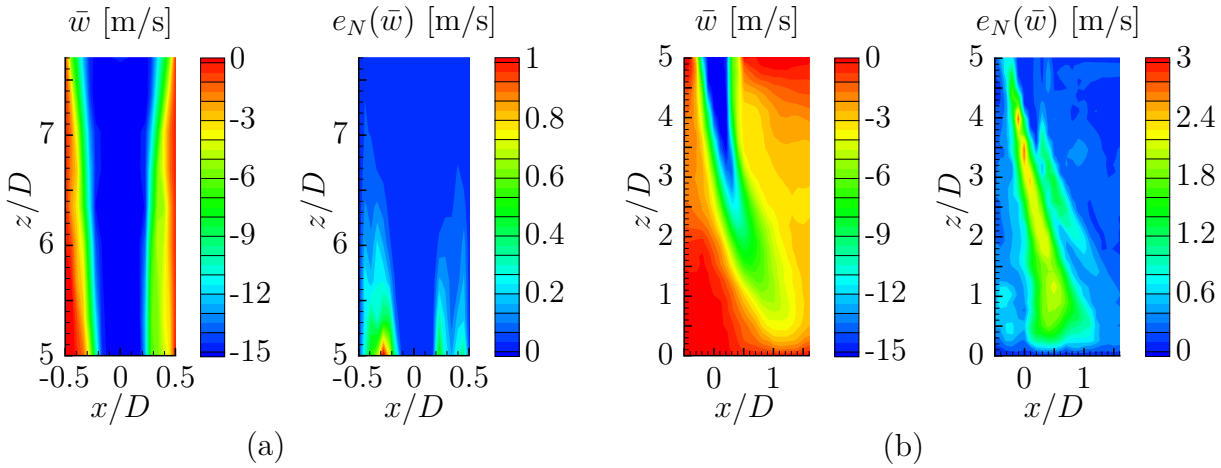

Figure 6.5: Contour plots of $\bar{w}$ and $e_N(\bar{w})$ within (a) and below (b) nozzle 7 at $y/D = 0$ for grid factor 4

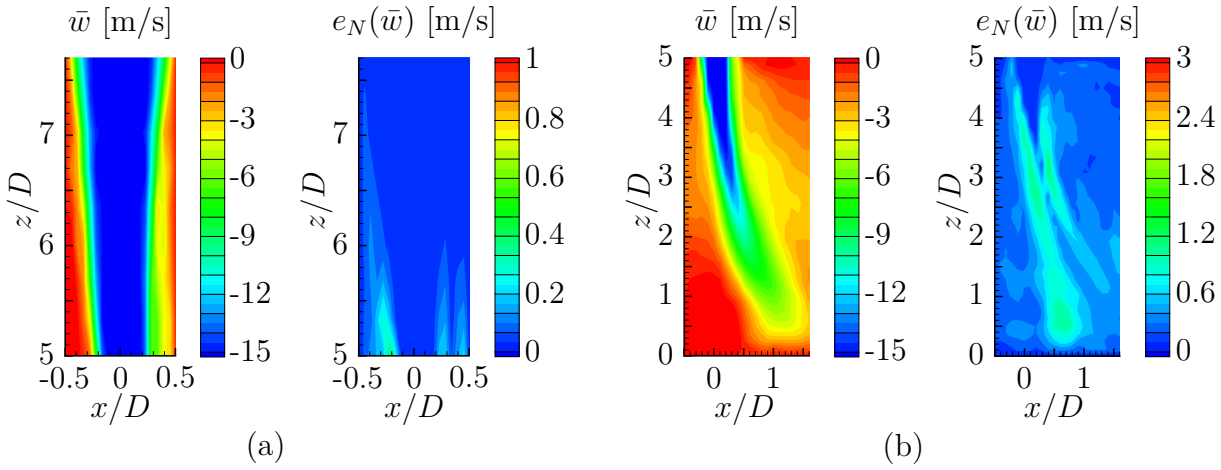

Figure 6.6: Contour plots of $\bar{w}$ and $e_N(\bar{w})$ within (a) and below (b) nozzle 7 at $y/D = 0$ for grid factor 5

6.2.4 Power Spectral Density Distributions

The *power spectral density* (PSD) distribution gives an insight on how the power of a certain quantity, such as pressure or velocity, is distributed over the frequency of the turbulent fluctuations. It has properties that are similar to the energy spectrum (see

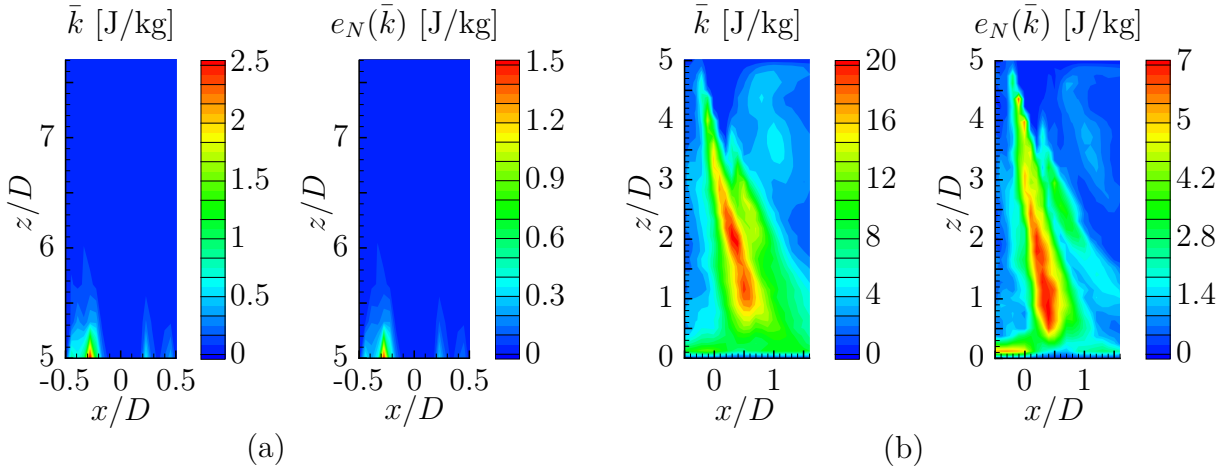

Figure 6.7: Contour plots of $\bar{k}$ and $e_N(\bar{k})$ within (a) and below (b) nozzle 7 at $y/D = 0$ for grid factor 4

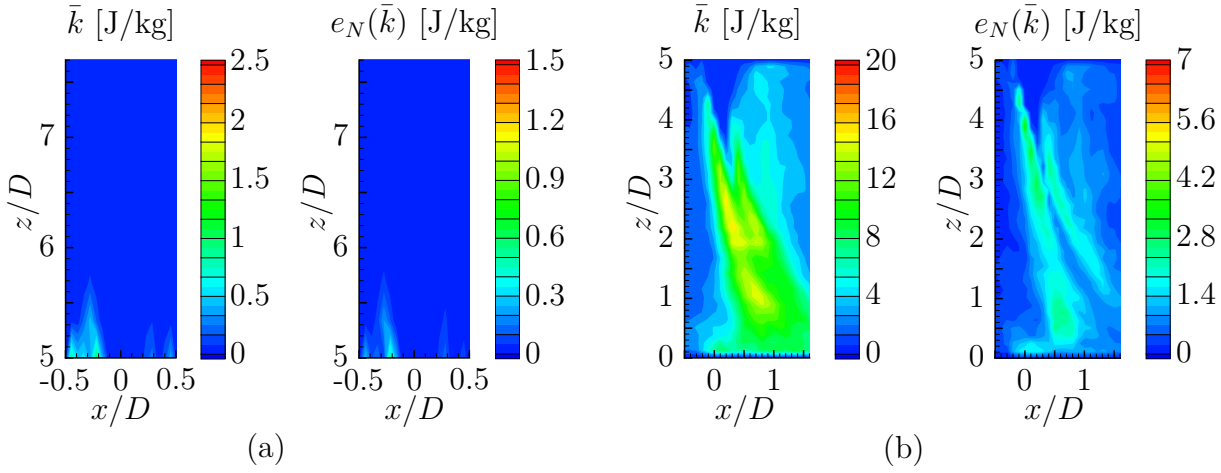

Figure 6.8: Contour plots of $\bar{k}$ and $e_N(\bar{k})$ within (a) and below (b) nozzle 7 at $y/D = 0$ for grid factor 5

Section 2.2.2) and provides further information about the turbulent character of the flow at a certain position in the domain. In this case, the PSD distributions of the z-component w of the velocity vector are studied for three positions (A, B and C) within as well as three positions (D, E and F) below nozzle 7. A visualization and the coordinates of these positions are given in Figure 6.9.

An estimate of the PSD distributions is computed using Welch's method [41] and the signal processing software *SciPy* (settings: nPerSeg = 13,333, window = hann). The resulting PSD are plotted over a non-dimensional frequency $f \cdot t_c$ in Figures 6.10 and 6.11 for grid factors 4 and 5. Additionally, the respective cut-off frequencies and $\sim f^{-\frac{5}{3}}$-lines are provided. The characteristic time t_c is based on l_{nozzle} and the averaged z-velocity

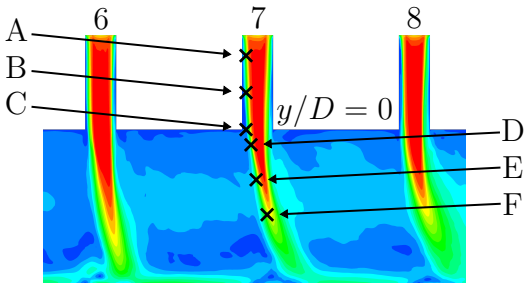

A: $\left(-0.39; 0; 7.03\right)^\top$ D: $\left(-0.20; 0; 4.49\right)^\top$

B: $\left(-0.39; 0; 6.01\right)^\top$ E: $\left(0; 0; 3.20\right)^\top$

C: $\left(-0.39; 0; 5\right)^\top$ F: $\left(0.30; 0; 1.91\right)^\top$

Figure 6.9: Visualization and coordinates $\left(x/D; y/D; z/D\right)^\top$ of positions A, B, C, D, E and F

$\bar{w}_{nozzle7}$ within nozzle 7. The cut-off frequency f_{cut} is based on Δ_{cut} and $\bar{w}$ at the respective positions.

$$t_c = \frac{l_{nozzle}}{\bar{w}_{nozzle7}} \qquad f_{cut} = \frac{\bar{w}}{2\pi \cdot \Delta_{cut}} \tag{6.13}$$

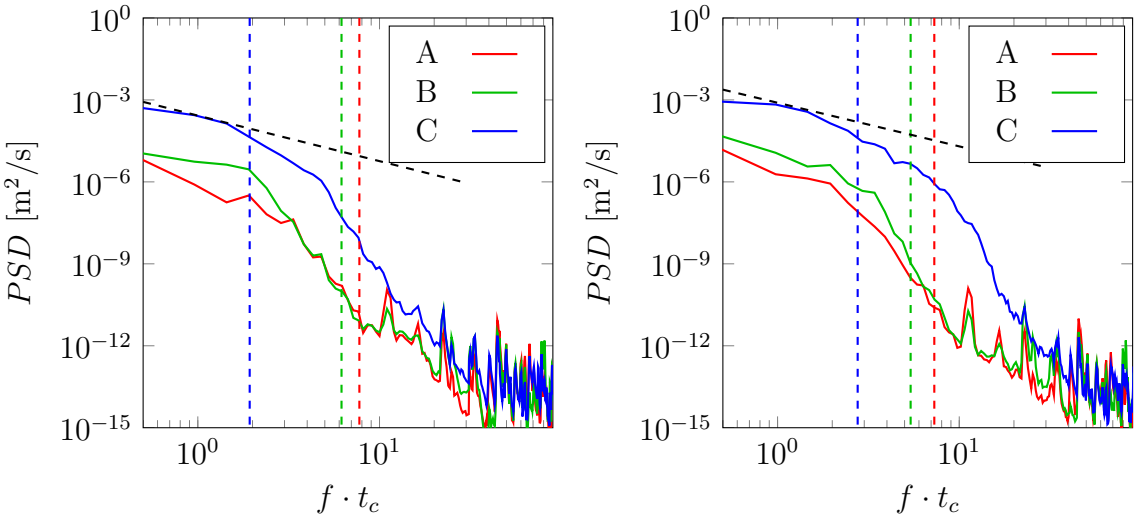

Figure 6.10: PSD distributions based on the z-component w of the velocity vector for positions A, B and C for grid factors 4 (a) and 5 (b). Dashed line (black): $\sim f^{-\frac{5}{3}}$, Dashed line (coloured): Cut-off frequency f_{cut} at respective position

At positions E and F, a relatively large inertial sub-range (see Section 2.2.2) becomes apparent where the PSD distributions are parallel to the $\sim f^{-\frac{5}{3}}$-lines. The inertial sub-range is considerably smaller at positions A, B, C and D. This phenomenon applies to grid factor 4 as well as grid factor 5 with latter showing a slightly larger inertial sub-range. Therefore, the PSD distributions indicate fully developed turbulence at positions E and F and less developed turbulence at positions A, B, C and D, which correlates to the

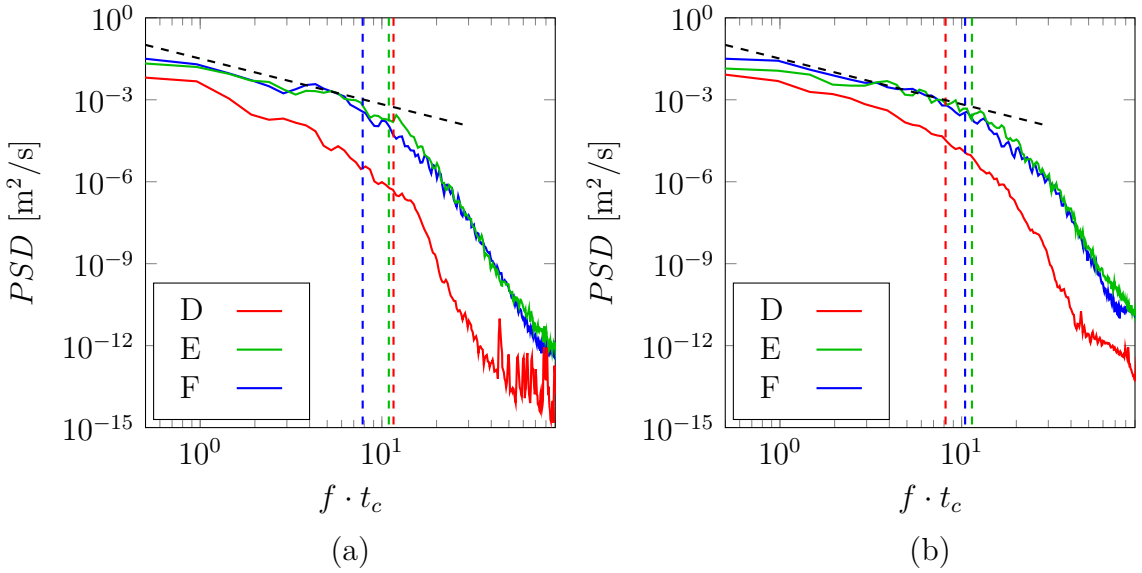

Figure 6.11: PSD distributions based on the z-component w of the velocity vector for positions D, E and F for grid factors 4 (a) and 5 (b). Dashed line (black): $\sim f^{-\frac{5}{3}}$, Dashed line (coloured): Cut-off frequency f_{cut} at respective position

turbulent kinetic energy distributions from Section 6.2.3. It should be noted, however, that there is a transition from isotropic three-dimensional turbulence to two-dimensional turbulence in the near-wall region. As a consequence, fully developed turbulence can be present at positions A, B and C despite the inertial sub-range not being parallel to $\sim f^{-\frac{5}{3}}$, but to $\sim f^{-3}$ or $\sim f^{-4}$ instead [15].

6.3 Velocity Field

In this section, the velocity fields of the LES and RANS studies are compared with each other. Figure 6.12 shows contour plots of the velocity fields and streamlines at nozzles 6, 7 and 8 for RANS study B (Figure 6.12a) and the LES study (Figure 6.12b). The Favre-averaged velocity magnitude $|\tilde{u}|$ is scaled with $w_{inlet} = 10.263$ m/s, which is obtained from Equation 4.1.

For the LES study, the boundary layer within the nozzle and therefore the center velocities of the free jets are larger compared to the RANS study. However, the RANS study shows larger potential cores that reach further towards the target plate. The reason for this could be a more intensive mixing in the shear layer of the LES study, which results in a stronger deceleration of its free jets. The streamlines indicate a stronger effect of cross-

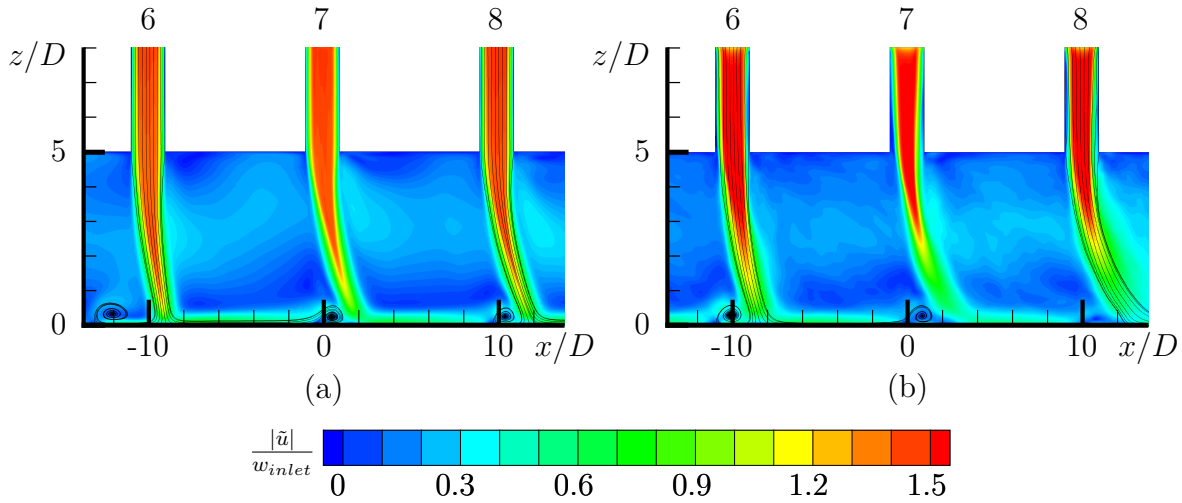

Figure 6.12: Contour plots of the Favre-averaged scaled velocity magnitude $|\tilde{u}|$ at nozzles 6, 7 and 8 with streamlines at $y/D = 0$ for RANS study B with grid factor 4 and inflow profiles (a) and the LES study with grid factor 5 (b)

flow on jet deflection for the LES due to the lower jet momentum in the stagnation region. In total, both studies show similar flow fields with different jet velocities and potential core sizes, whose main causes lie in the the flow regimes within the nozzles and the shear layers.

6.4 Heat Transfer

This section provides detailed information about the heat transfer characteristics resulting from the LES study. Both area averaged and spanwise averaged Nusselt number distributions are used for this purpose. They are compared to the results obtained from both RANS studies with the area averaged Nusselt numbers being additionally compared to correlations from the literature.

6.4.1 Area Averaged Nusselt Numbers

Figure 6.13a shows the target plate and heating plate averaged Nusselt numbers (see Section 5.3.1) of the LES study and both RANS studies. Additionally, Figure 6.13b provides target plate averaged Nusselt numbers based on correlations from References [18, 19, 22, 26, 30], in which similar test cases were studied experimentally. The correlations are applied to the considered impinging jet configuration in order to validate the simulation data. They consist of empirically determined equations that provide a relation between

the target plate averaged Nusselt number, Re_{inlet}, Pr and several geometrical parameters (see Chapter 4).

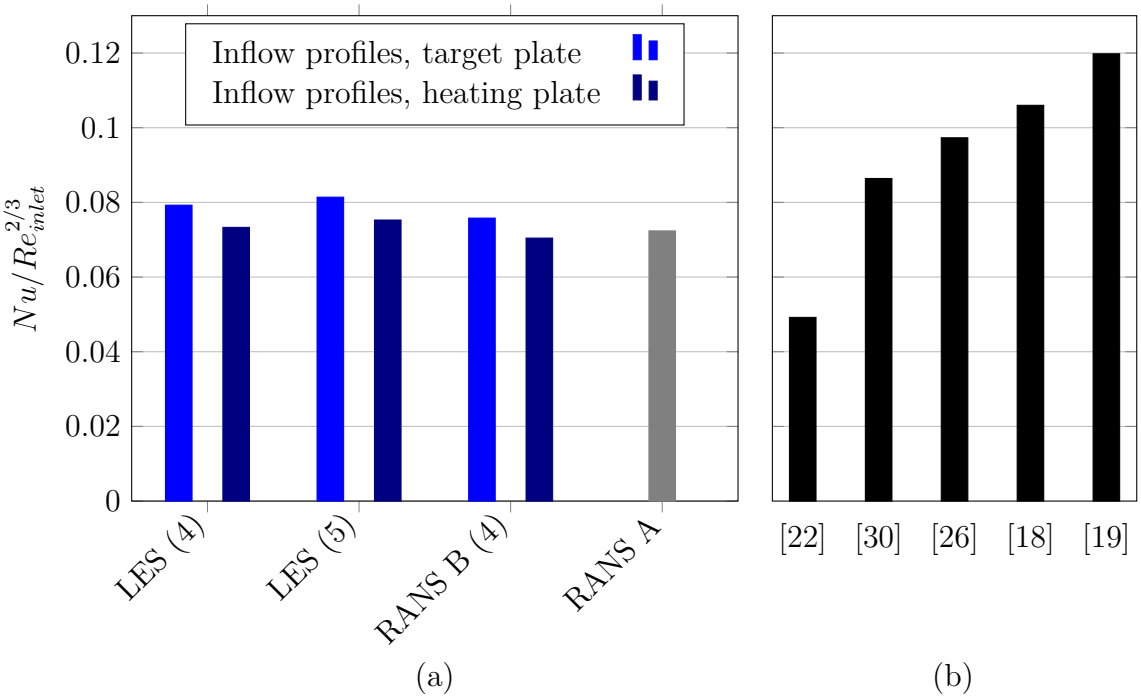

Figure 6.13: Target plate and heating plate averaged Nusselt numbers for the LES study (grid factors 4 and 5), RANS study B (grid factor 4, inflow profiles) and RANS study A (heating plate averaged) (a) as well as target plate averaged Nusselt numbers based on correlations from the literature (b)

The area averaged Nusselt numbers from the LES study are slightly higher than the Nusselt numbers from the RANS studies. However, the LES results show the same effect of higher target plate averaged Nusselt numbers compared to the heating plate averaged Nusselt numbers, which is discussed in Section 5.3.1. Since the literature correlations are related to the target plate, only the target plate averaged Nusselt numbers from the LES study and RANS study B can be used for comparison. While the results from the LES studies and RANS study B are in good agreement with the correlations from Reference [30], there is a considerably large deviation to the correlations from References [22], [26], [18] and [19]. In total, however, the results are sufficient as they clearly lie within the rather broad spectrum of correlations.

6.4.2 Spanwise Averaged Nusselt Number Distributions

The heating plate spanwise averaged Nusselt number distributions for the LES study and both RANS studies are given in Figure 6.14. Apart from the stagnation points of jets 6,7 and 9, the distributions of both LES are in good agreement with each other. However, they differ significantly from the distributions of both RANS studies. The deviation from RANS study B is smaller compared to the deviation from RANS study A, since the LES study and RANS study B both use same numerical grids. In area average (see Section 6.4.1), these deviations are compensated, as the Nusselt numbers from the LES study are higher in the fountain flow region and lower at the stagnation points compared to the RANS study. As mentioned in Section 6.3, the LES predicts smaller potential cores causing reduced flow speeds and therefore heat transfer in the stagnation regions. The assumption of more intensive mixing in the shear layer of the LES may be a reason for increased heat transfer in the ambient fluid, i.e., the fountain flow region.

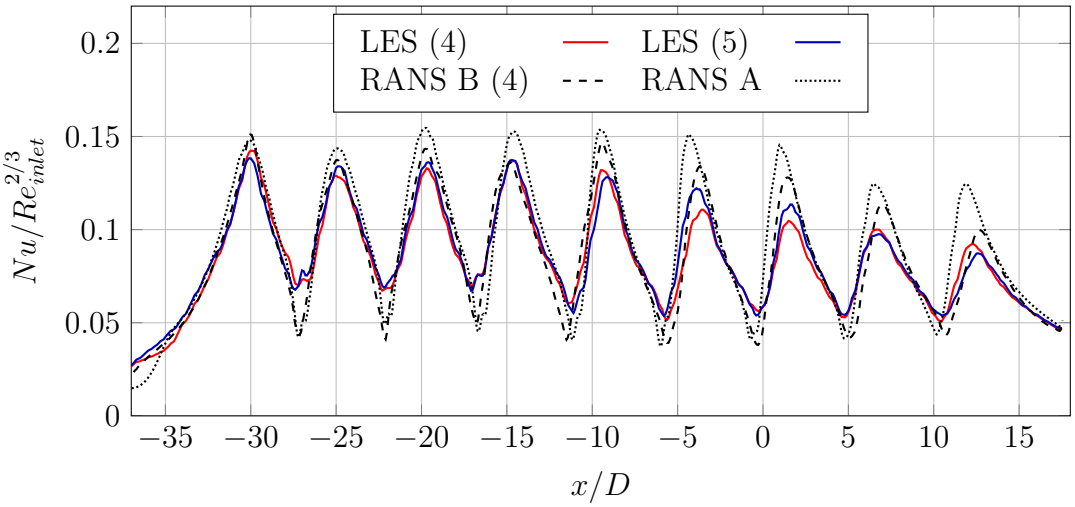

Figure 6.14: Heating plate spanwise averaged Nusselt number distributions for the LES study (grid factors 4 and 5), RANS Study B (grid factor 4, inflow profiles) and RANS Study A

7 Conclusion

Several RANS simulations and LES were conducted for a generic configuration of multiple impinging jets using the CFD solver TRACE. As a result, extensive numerical data particularly relating to the heat transfer processes within this configuration was obtained.

The RANS simulations fulfil all requirements concerning grid resolution, residuals and grid convergence. The scalability of the Nusselt number with the Reynolds number and thus the compensation of changes in mass flow was confirmed for this test case. Considering future experimental studies, the occurrence of slight deviations in mass flow or heat flux can therefore be regarded as non-critical.

The LES were conducted with grid resolutions that were found to be suitable. However, large sampling errors suggest that the velocity and the turbulent kinetic energy are not sufficiently converged within the time limit of this study.

To achieve statistical convergence, the LES have to be continued to a larger number of through flows. The plenum of the original test case was not included in the RANS and LES setups. Instead, laminar inflow boundary conditions were used, which is presumed to be the reason for the absence of fully developed turbulence within the nozzles. Therefore, further LES should be carried out with a plenum to verify this assumption.

In total, the LES study is presumed to predict the local Nusselt numbers more accurately than the RANS study. This is justified by the fact that RANS simulations are highly dependent on model assumptions, which are potential sources of modelling errors (e.g., in the stagnation region). To confirm this hypothesis, the numerical data obtained from the RANS and LES studies has to be validated experimentally. A corresponding experiment with an identical test case is currently being carried out at the DLR, whose evaluation will be part of future studies.

Bibliography

[1] J. D. Anderson JR. *Computational Fluid Dynamics: The Basics with Applications*. New York, United States of America: McGraw-Hill, 1995. ISBN: 0-07-001685-2.

[2] *ANSYS Fluent Theory Guide*. 15th ed. Canonsburg, United States of America, 2013.

[3] M. Bergmann and C. Morsbach. "DRAFT: Uncertainty-aware large eddy simulation of the T106C low-pressure turbine cascade". In: *American Society of Mechanical Engineers Journal* (2021, unpublished).

[4] J. Blazek. *Computational Fluid Dynamics: Principles and Applications*. Amsterdam, The Netherlands: Elsevier, 2001. ISBN: 0080430090.

[5] J. Boussinesq. "Essai sur la théorie des eaux courantes". In: *Mémoires présentes par divers savants à l'Académie des Sciences* 46 (1877).

[6] R. Brakmann. "Increasing Heat Transfer in Convective Cooling Systems with Optimized Surface Structures". Doctoral thesis. Stuttgart: University of Stuttgart, 2017.

[7] I. B. Celik et al. "Journal of Fluids Engineering Editorial Policy Statement on the Control of Numerical Accuracy: Procedure for Estimation and Reporting of Uncertainty Due to Discretization in CFD Applications". In: *Journal of Fluids Engineering* 130 (2008).

[8] L. Davidson. *Fluid mechanics, turbulent flow and turbulence modeling*. Göteborg, Sweden, 2016.

[9] A. Dewan, R. Dutta, and B. Srinivasan. "Recent Trends in Computation of Turbulent Jet Impingement Heat Transfer". In: *Heat Transfer Engineering* 33.4-5 (2012), pp. 447–460. ISSN: 0145-7632. DOI: 10.1080/01457632.2012.614154.

[10] A. Dewan, R. Dutta, and B. Srinivasan. "Recent Trends in Computation of Turbulent Jet Impingement Heat Transfer". In: *Heat Transfer Engineering* 33.4-5 (2012), pp. 447–460. ISSN: 0145-7632. DOI: 10.1080/01457632.2012.614154.

[11] F. Ducros, F. Nicoud, and T. Poinsot. *Wall-Adapting Local Eddy-Viscosity Models for Simulations in Complex Geometries*. 1998.

[12] A. Einstein. “Die Grundlage der allgemeinen Relativitätstheorie”. In: *Annalen der Physik* 49 (1916), pp. 769–822.

[13] A. Favre. “Equations des gaz turbulents compressibles”. In: *Journal de Méchanique* 4 (1965), pp. 361–421.

[14] J. H. Ferziger, M. Perić, and R. L. Street. *Computational Methods for Fluid Dynamics*. Cham: Springer International Publishing, 2020. ISBN: 978-3-319-99691-2. DOI: 10.1007/978-3-319-99693-6.

[15] J. Fröhlich. *Large Eddy Simulation turbulenter Strömungen*. 1st ed. Teubner, 2006. ISBN: 3835101048. DOI: 10.1007/978-3-8351-9051-1.

[16] J. Fröhlich et al. “Highly resolved large-eddy simulation of separated flow in a channel with streamwise periodic constrictions”. In: *Journal of Fluid Mechanics* 526 (2005), pp. 19–66. DOI: 10.1017/S0022112004002812.

[17] M. García-Villalba, H. Kuerten, and M. V. Salvetti. *Direct and Large Eddy Simulation XII*. Vol. 27. Cham: Springer International Publishing, 2020. ISBN: 978-3-030-42821-1. DOI: 10.1007/978-3-030-42822-8.

[18] R. Gardon and J. Cobonpue. “Heat Transfer Between a Flat Plate and Jets of Air Impinging on It”. In: *International Developments in Heat Transfer* (1962), pp. 454–460.

[19] S. Garimella and V. Schroeder. “Local heat transfer distributions in confined multiple air jet impingement”. In: *Journal of Electronic Packaging* 123 (2001), pp. 165–172.

[20] E. Garnier, N. Adams, and P. Sagaut. *Large Eddy Simulation for Compressible Flows*. Dordrecht, The Netherlands: Springer Netherlands, 2009. ISBN: 978-90-481-2818-1. DOI: 10.1007/978-90-481-2819-8.

[21] J. W. Gauntner, J. N. B. Livingood, and P. Hrycak. *Survey of Literature on Flow Characteristics of a Single Turbulent Jet Impinging on a Flat Plate*. Cleveland, Ohio, United States of America, 1970.

[22] R. J. Goldstein and W. S. Seol. “Heat transfer to a row of impinging circular air jets including the effect of entrainment”. In: *International Journal of Heat and Mass Transfer* 34 (1991), pp. 2133–2147. ISSN: 00179310.

[23] T. Guo et al. “Axisymmetric wall jet development in confined jet impingement”. In: *Physics of Fluids* 29 (2017), pp. 1–12. ISSN: 1070-6631. DOI: 10.1063/1.4975394.

[24] J.-C. Han. "Recent Studies in Turbine Blade Cooling?" In: *The International Journal of Rotating Machinery* 10.6 (2004), pp. 443–457. ISSN: 1023-621X. DOI: 10.1080/10236210490503978.

[25] Y. Huang, S. V. Ekkad, and J.-C. Han. "Detailed Heat Transfer Distributions Under an Array of Orthogonal Impinging Jets". In: *Journal of Thermophysics and Heat Transfer* 12.1 (1998), pp. 73–79. ISSN: 0887-8722. DOI: 10.2514/2.6304.

[26] A. M. Huber and R. Viskanta. "Effect of jet–jet spacing on convective heat transfer to confined, impinging arrays of axisymmetric jets". In: *International Journal of Heat and Mass Transfer* 37 (1994), pp. 2859–2869. ISSN: 00179310.

[27] F. P. Incropera. *Fundamentals of heat and mass transfer*. 6th ed. Hoboken NJ: John Wiley, 2007. ISBN: 9780471457282.

[28] U. K S, S. Kurian, and J. Johnson. "Study of Jet Impingement Heat Transfer". In: *International Research Journal of Engineering and Technology (IRJET)* 5 (2018), pp. 1657–1664.

[29] B. Lakshminarayana. *Fluid Dynamics and Heat Transfer of Turbomachinery*. United States of America: John Wiley, 1996. ISBN: 0-471-85546-4.

[30] H. Martin et al. "Heat and Mass Transfer between Impinging Gas Jets and Solid Surfaces". In: *Advances in Heat Transfer* 13 (1977), pp. 1–60.

[31] F. R. Menter. "Two-equation Eddy-Viscosity Turbulence Models for Engineering Applications". In: *AIAA Journal* 32 (1994), pp. 1598–1605.

[32] H. Oertel, M. Böhle, and T. Reviol. *Strömungsmechanik*. Wiesbaden: Springer Fachmedien Wiesbaden, 2015. ISBN: 978-3-658-07785-3. DOI: 10.1007/978-3-658-07786-0.

[33] O. Reynolds. "On the dynamical theory of incompressible viscous fluids and the determination of the criterion". In: *Philosophical Transactions of the Royal Society of London* 186 (1895), pp. 123–164. DOI: 10.1098/rsta.1895.0004.

[34] P. Roe. "Approximate Riemann solvers, parameter vectors, and difference schemes". In: *Journal of Computational Physics* 43.2 (1981), pp. 357–372. DOI: 10.1016/0021-9991(81)90128-5.

[35] M. T. Schobeiri. *Gas Turbine Design, Components and System Design Integration*. Cham: Springer International Publishing, 2019. ISBN: 978-3-030-23972-5. DOI: 10.1007/978-3-030-23973-2.

[36] R. Schwarze. *CFD-Modellierung*. Berlin, Heidelberg: Springer Berlin Heidelberg, 2013. ISBN: 978-3-642-24377-6. DOI: 10.1007/978-3-642-24378-3.

[37] J. Smagorinsky. "General Circulation Experiments with the Primitive Equations". In: *Monthly Weather Review* 91 (1963), pp. 99–164.

[38] J. H. Spurk and N. Aksel. *Fluid Mechanics*. Cham: Springer International Publishing, 2020. ISBN: 978-3-030-30258-0. DOI: 10.1007/978-3-030-30259-7.

[39] B. Vreman. "Direct and Large-Eddy Simulation of the Compressible Turbulent Mixing Layer". Dissertation. Twente, The Netherlands: University of Twente.

[40] B. Weigand and S. Spring. "Multiple Jet Impingement - A Review". In: *Heat Transfer Research* 42 (2011), pp. 101–142.

[41] P. D. Welch. "The Use of Fast Fourier Transform for the Estimation of Power Spectra: A Method Based on Time Averaging Over Short, Modified Periodograms". In: *IEEE Transactions on Audio and Electroacoustics* 15 (1967), pp. 70–73.

[42] D. C. Wilcox. *Turbulence Modeling for CFD*. 3rd ed. California, United States of America: DCW Industries, 2006. ISBN: 978-1-928729-08-2.

[43] L. Yang et al. "Experimental and numerical investigation of unsteady impingement cooling within a blade leading edge passage". In: *International Journal of Heat and Mass Transfer* 71 (2014), pp. 57–68. ISSN: 00179310. DOI: 10.1016/j.ijheatmasstransfer.2013.12.006.

[44] N. Zuckerman and N. Lior. "Impingement Heat Transfer: Correlations and Numerical Modeling". In: *Journal of Heat Transfer* 127.5 (2005), pp. 544–552. ISSN: 0022-1481. DOI: 10.1115/1.1861921.

A Computational Methods

A.1 Wilcox k-ω Model

Modelling coefficients a and a^* [2]:

$$\alpha = \frac{\alpha_\infty}{\alpha^*}\left(\frac{\alpha_0 + Re_T/R_\omega}{1 + Re_T/R_\omega}\right) \qquad \alpha^* = \alpha^*_\infty\left(\frac{\alpha^*_0 + Re_T/R_k}{1 + Re_T/R_k}\right) \qquad Re_T = \frac{\rho k}{\mu\omega} \tag{A.1}$$

Dissipation of k [2]:

$$Y_k = \rho\beta^* f_{\beta^*} k\omega \tag{A.2}$$

$$\beta^* = \beta^*_i\left[1 + \zeta^* F(Ma_T)\right] \qquad \beta^*_i = \beta^*_\infty\left(\frac{4/15 + (Re_T/R_\beta)^4}{1 + (Re_T/R_\beta)^4}\right) \tag{A.3}$$

$$f_{\beta^*} = \begin{cases} 1 & \chi_k \leq 0 \\ \frac{1+680\chi_k^2}{1+400\chi_k^2} & \chi_k > 0 \end{cases} \qquad \chi_k \equiv \frac{1}{\omega^3}\frac{\partial k}{\partial x_j}\frac{\partial \omega}{\partial x_j} \tag{A.4}$$

Dissipation of ω [2]:

$$Y_\omega = \rho\beta f_\beta \omega^2 \tag{A.5}$$

$$\beta = \beta_i\left[1 - \frac{\beta^*_i}{\beta_i}\zeta^* F(Ma_T)\right] \tag{A.6}$$

$$f_\beta = \frac{1 + 70\chi_\omega}{1 + 80\chi_\omega} \qquad \chi_\omega = \left|\frac{\Omega_{ij}\Omega_{jk}S_{ki}}{(\beta^*_\infty\omega)^3}\right| \qquad \Omega_{ij} = \frac{1}{2}\left(\frac{\partial u_i}{\partial x_j} - \frac{\partial u_j}{\partial x_i}\right) \tag{A.7}$$

Compressibility correction [2]:

$$F(Ma_T) = \begin{cases} 0 & Ma_T \leq Ma_{T0} \\ Ma_T^2 - Ma_{T0}^2 & Ma_T > Ma_{T0} \end{cases} \tag{A.8}$$

A.2 Shear Stress Transport k-ω Model

Blending functions [2]:

$$F_1 = \tanh\left(\min\left[\max\left(\frac{\sqrt{k}}{0.09\omega y}, \frac{500\mu}{\rho y^2 \omega}\right), \frac{4\rho k}{\sigma_{\omega,2} D_\omega^+ y^2}\right]\right) \tag{A.9}$$

$$F_2 = \tanh\left(\max\left[2\frac{\sqrt{k}}{0.09\omega y}, \frac{500\mu}{\rho y^2 \omega}\right]\right) \tag{A.10}$$

$$D_\omega^+ = \max\left[2\rho\frac{1}{\sigma_{\omega,2}}\frac{1}{\omega}\frac{\partial k}{\partial x_j}\frac{\partial \omega}{\partial x_j}, 10^{-10}\right] \tag{A.11}$$

Modelling coefficients σ_k and σ_ω [2]:

$$\sigma_k = \frac{1}{F_1/\sigma_{k,1} + (1-F_1)/\sigma_{k,2}} \qquad \sigma_\omega = \frac{1}{F_1/\sigma_{\omega,1} + (1-F_1)/\sigma_{\omega,2}} \tag{A.12}$$

Modelling coefficients a and a^*: See Equation A.1. Note that α_∞ is not a constant and thus has to be calculated instead.[2]

$$\alpha_\infty = F_1\alpha_{\infty,1} + (1-F_1)\alpha_{\infty,2} \tag{A.13}$$

$$\alpha_{\infty,1} = \frac{\beta_{i,1}}{\beta_\infty^*} - \frac{\kappa^2}{\sigma_{\omega,1}\sqrt{\beta_\infty^*}} \qquad \alpha_{\infty,2} = \frac{\beta_{i,2}}{\beta_\infty^*} - \frac{\kappa^2}{\sigma_{\omega,2}\sqrt{\beta_\infty^*}} \qquad \kappa = 0.41 \tag{A.14}$$

Dissipation of k (for β^* see Equation A.3) [2]:

$$Y_k = \rho\beta^* k\omega \tag{A.15}$$

Dissipation of ω (for β see Equation A.6, note that β_i is not a constant) [2]:

$$Y_\omega = \rho\beta\omega^2 \qquad \beta_i = F_1\beta_{i,1} + (1-F_1)\beta_{i,2} \tag{A.16}$$

Cross-diffusion term D_ω [2]:

$$D_\omega = 2(1-F_1)\rho\frac{1}{\omega\sigma_{\omega,2}}\frac{\partial k}{\partial x_j}\frac{\partial \omega}{\partial x_j} \tag{A.17}$$

B Test Case and Numerical Setup

B.1 Mesh

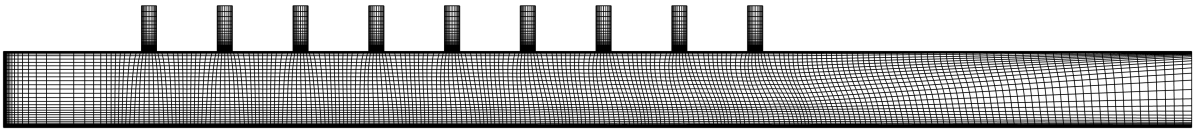

Figure B.1: Side view of the block-structured grid of Study B (grid factor 1)

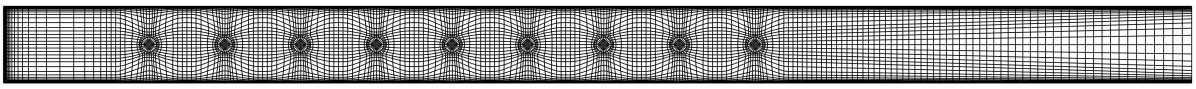

Figure B.2: Top view of the block-structured grid of Study B (grid factor 1)

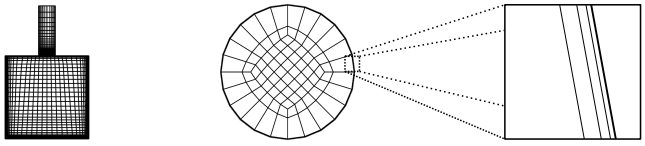

(a) (b) (c)

Figure B.3: Front view of the block-structured grid of Study B (a), top view of the inflow surface (b) and detailed view of the near-wall grid of the inflow surface (c) (grid factor 1)

Table B.4: Number of grid cells for the duct and the nozzles (grid factor 1)

Duct	Nozzle
x-direction: 59	Circumferential direction: 24
y-direction: 42	z-direction: 39
z-direction: 42	

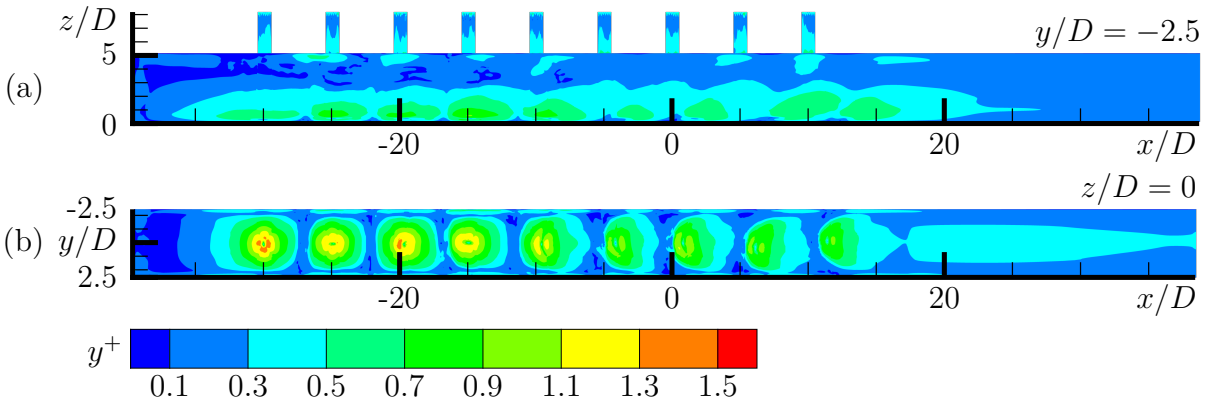

Figure B.5: Side view (a) and target plate view (b) of a non-dimensional distance wall coordinate y^+ plot for the node that is next to the wall (grid factor 4, inflow profiles)

C RANS Simulation

C.1 Solver Settings

Table C.1: Solver settings for the RANS simulations

General solver settings	
Solver mode	Non-linear
Simulation mode	Steady
Boundary condition method	Riemann
Spatial discretization	
Scheme	Fromm
Accuracy	Second order
Entropy fix	$1{\cdot}10^{-6}$
Limiter	Van Albada
Temporal discretization	
Solution method	Predictor/corrector
CFL	Ramp: $CFL = 1$ at time step 1, $CFL = 50$ at time step 100
Reference state	
Reference length	0.0076 m
Reference pressure	102,037 Pa
Reference temperature	298.2 K

C.2 Residuals

Normalization procedure for L1 residuals within TRACE with the number of cells N, the number of equations $n_{equations}$, the pseudo time step $\Delta\tau$, the cell volume V, the CFL number and the residual vector R:

$$\text{ResidualL1} = \frac{1}{N}\sum_{j}^{N}\sum_{i}^{n_{equations}}\left|\frac{\Delta\tau_j}{V_j \cdot CFL}R_i^j\right| \tag{C.1}$$

C.3 GCI Procedure

The following procedure can be applied to any flow variable ϕ. A representative cell size h is introduced with the cell volume ΔV_i and the total number of cells N.[7]

$$h = \left(\frac{1}{N}\sum_{i=1}^{N}\Delta V_i\right)^{\frac{1}{3}} \tag{C.2}$$

The minimum value of 2 is recommended for the grid refinement factor $r = \frac{h_{coarse}}{h_{fine}}$. The indices 1,2 and 3 stand for the fine, medium and coarse grid.[7]

$$\text{By definition: } h_1 < h_2 < h_3 \tag{C.3}$$

$$r_{21} = \frac{h_2}{h_1} \qquad r_{32} = \frac{h_3}{h_2} \tag{C.4}$$

$$\varepsilon_{21} = \phi_2 - \phi_1 \qquad \varepsilon_{32} = \phi_3 - \phi_2 \tag{C.5}$$

The apparent order p is calculated by applying a fix-point iteration to Equations C.6, C.7 and C.8 with Equation C.6 as an initial guess [7].

$$p = \frac{1}{\log(r_{21})}\left|\ln\left(\left|\frac{\varepsilon_{32}}{\varepsilon_{21}}\right|\right) + q(p)\right| \tag{C.6}$$

$$q(p) = \ln\left(\frac{r_{21}^p - s}{r_{32}^p - s}\right) \tag{C.7}$$

$$s = 1 \cdot \text{sign}\left(\frac{\varepsilon_{32}}{\varepsilon_{21}}\right) \tag{C.8}$$

Extrapolated values ϕ_{ext}^{21} and ϕ_{ext}^{32} of general flow variable (as recommended, the mean value of p is used) ϕ [7]:

$$\phi_{ext}^{21} = \frac{r_{21}^{p_{mean}}\phi_1 - \phi_2}{r_{21}^{p_{mean}} - 1} \qquad \phi_{ext}^{32} = \frac{r_{32}^{p_{mean}}\phi_2 - \phi_3}{r_{32}^{p_{mean}} - 1} \tag{C.9}$$

Approximated relative error e_a^{21}, extrapolated relative error e_{ext}^{21} and fine-grid convergence index GCI_{fine}^{21} [7]:

$$e_a^{21} = \left|\frac{\phi_1 - \phi_2}{\phi_1}\right| \tag{C.10}$$

$$e_{ext}^{21} = \left|\frac{\phi_{ext}^{12} - \phi_1}{\phi_{ext}^{12}}\right| \tag{C.11}$$

$$GCI_{fine}^{21} = \frac{1.25e_a^{21}}{r_{21}^{p_{mean}} - 1} \tag{C.12}$$

Extrapolated absolute error $e_{ext,abs}^{21}$:

$$e_{ext,abs}^{21} = e_{ext}^{21} \cdot \phi \tag{C.13}$$

D Large Eddy Simulation

D.1 Solver Settings

Table D.1: Solver settings for the large eddy simulations

General solver settings	
Solver mode	Non-linear
Simulation mode	Unsteady
Time steps per period	1,024
Frequency	13,020 Hz
Boundary condition method	Riemann (exception: Unsteady 1D characteristics for outlet)
Spatial discretization	
Scheme	Third order
Accuracy	Second order
Entropy fix	$1{\cdot}10^{-6}$
Limiter	Off
Temporal discretization	
Scheme	Explicit Runge Kutta
Accuracy	Third order
Reference state	
Reference length	0.0076 m
Reference pressure	102,037 Pa
Reference temperature	298.2 K